



**HAL**  
open science

## **A multi-technique characterisation of cronstedtite synthesized by iron-clay interaction in a step by step cooling procedure**

Isabella Pignatelli, Enrico Mugnaioli, J. Hybler, Régine Mosser-Ruck, Michel Cathelineau, Nicolas Michau

### **► To cite this version:**

Isabella Pignatelli, Enrico Mugnaioli, J. Hybler, Régine Mosser-Ruck, Michel Cathelineau, et al.. A multi-technique characterisation of cronstedtite synthesized by iron-clay interaction in a step by step cooling procedure. *Clays and Clay Minerals*, 2013, 61 (4), pp.277-289. <10.1346/CCMN.2013.0610408>. <hal-01876737>

**HAL Id: hal-01876737**

**<https://hal.univ-lorraine.fr/hal-01876737v1>**

Submitted on 18 Sep 2018

**HAL** is a multi-disciplinary open access archive for the deposit and dissemination of scientific research documents, whether they are published or not. The documents may come from teaching and research institutions in France or abroad, or from public or private research centers.

L'archive ouverte pluridisciplinaire **HAL**, est destinée au dépôt et à la diffusion de documents scientifiques de niveau recherche, publiés ou non, émanant des établissements d'enseignement et de recherche français ou étrangers, des laboratoires publics ou privés.



HAL Authorization

# Clays and Clay Minerals

## A multi-technique characterisation of cronstedtite synthesized by iron-clay interaction in a step by step cooling procedure

--Manuscript Draft--

<b>Manuscript Number:</b>	CCM-748R1
<b>Full Title:</b>	A multi-technique characterisation of cronstedtite synthesized by iron-clay interaction in a step by step cooling procedure
<b>Short Title:</b>	Synthesis of cronstedtite by iron-clay interaction
<b>Article Type:</b>	Article
<b>Section/Category:</b>	
<b>Keywords:</b>	Cronstedtite; MDO polytypes; radioactive waste storage; experimental iron-clay interaction.
<b>Corresponding Author:</b>	Isabella Pignatelli GeoRessources Vandœuvre-lès-Nancy, FRANCE
<b>Corresponding Author Secondary Information:</b>	
<b>Corresponding Author's Institution:</b>	GeoRessources
<b>Corresponding Author's Secondary Institution:</b>	
<b>First Author:</b>	Isabella Pignatelli
<b>First Author Secondary Information:</b>	
<b>Order of Authors:</b>	Isabella Pignatelli Enrico Mugnaioli, doctoral degree Jiri Hybler, doctoral degree Régine Mosser-Ruck, doctoral degree Michel Cathelineau, professor Nicolas Michau, doctoral degree
<b>Order of Authors Secondary Information:</b>	
<b>Abstract:</b>	<p>The cooling of steel containers in radioactive waste storages has been simulated by an original step by step experiment from 90°C to 40°C. Among newly formed clay minerals observed in run products, cronstedtite has been undoubtedly identified by different analytical techniques (XRD, TEM and SEM). This is the first time that cronstedtite is so abundant and well-crystallized in an iron-clay interaction experiment. The supersaturation of experimental solutions with respect to cronstedtite is due to the availability of Fe and Si in solution, as a result of the dissolution of iron metal powder, quartz and in a minor amount other silicates. Cronstedtite crystals are characterized by various morphologies: pyramidal (truncated or not) with a triangular base and conic with a rounded or hexagonal cross-section. The pyramidal crystals occur more frequently and their polytypes (2M1, 1M, 3T) have been identified by selected area electron diffraction (SAED) patterns and by automated diffraction tomography (ADT). Cronstedtite is stable within the 90°-60°C temperature range. At temperature <math>\leq 50^\circ\text{C}</math>, cronstedtite crystals show evidences of alteration.</p>



24 crystallized in an iron-clay interaction experiment. The supersaturation of experimental  
25 solutions with respect to cronstedtite is due to the availability of Fe and Si in solution, as a  
26 result of the dissolution of iron metal powder, quartz and in a minor amount other silicates.  
27 Cronstedtite crystals are characterized by various morphologies: pyramidal (truncated or not)  
28 with a triangular base and conic with a rounded or hexagonal cross-section. The pyramidal  
29 crystals occur more frequently and their polytypes ( $2M_1$ ,  $1M$ ,  $3T$ ) were identified by selected  
30 area electron diffraction (SAED) patterns and by automated diffraction tomography (ADT).  
31 Cronstedtite is stable within the 90°-60°C temperature range. At temperature  $\leq 50^\circ\text{C}$ ,  
32 cronstedite crystals show evidences of alteration.

## 33 **KEYWORDS**

34 Cronstedtite, MDO polytypes, radioactive waste storage, experimental iron-clay interaction.

## 36 **INTRODUCTION**

37 This paper presents a multi-technique characterization of cronstedtite crystals formed from an  
38 original experimental procedure on iron-clay interactions. The choice of this experiment was  
39 driven by the need to evaluate the effects of a progressive decrease in temperature expected  
40 during the cooling of nuclear waste containers. First of all, a mineralogical assemblage was  
41 obtained after heating at 90°C an iron-clay mixture. Its retrograde evolution was thus  
42 simulated by a step by step cooling experiment between 90°C and 40°C. For the first time,  
43 single crystals of well-crystallized cronstedtite were observed in run products and accurately  
44 characterized. The temperature stability domain of cronstedtite was estimated on the basis of  
45 experimental evidence (occurrence and instability of crystals) and compared to literature data.  
46 This detailed mineralogical characterization of newly formed cronstedtite is useful to improve  
47 databases of the thermodynamic models.

## BACKGROUND

49 Cronstedtite is a T-O or 1:1 phyllosilicate, with a general formula  $(\text{Fe}^{2+}_{3-x} \text{Fe}^{3+}_x)(\text{Si}_{2-x}\text{Fe}^{3+}_x)\text{O}_5(\text{OH})_4$ , with  $0 < x < 0.8$  (Geiger *et al.*, 1983; Smrčok *et al.*, 1994; Hybler *et al.*, 2000; Hybler *et al.*, 2002; Kogure *et al.*, 2002), close to the initial ideal formula  $(\text{Fe}^{2+}_2 \text{Fe}^{3+})(\text{SiFe}^{3+})\text{O}_5(\text{OH})_4$  proposed by Hendricks (1939). Chemical analyses of cronstedtite also show that the octahedrally coordinated iron can be replaced by other cations as  $\text{Mg}^{2+}$ ,  $\text{Mn}^{2+}$ ,  $\text{Al}^{3+}$  (Fron del, 1962; Geiger *et al.*, 1983) and that the tetrahedral sites can also contain  $\text{Al}^{3+}$  (Geiger *et al.*, 1983; Hybler *et al.*, 2002). Cronstedtite forms a solid solution with greenalite  $(\text{Fe}^{2+}, \text{Fe}^{3+}, \text{Mg}, \square)_3(\text{Si}, \text{Al})_2\text{O}_5(\text{OH})_4$  (Guggenheim *et al.*, 1982), another Fe-rich layer silicate, from which it differs by the presence of ferric iron in tetrahedral coordination.

58 Like other trioctahedral T-O phyllosilicates, standard polytypes of cronstedtite can be classified in four subfamilies, identical with Bailey's (1969) groups: A ( $1M$ ,  $2M_1$ ,  $3T$  polytypes), B ( $2O$ ,  $2M_2$ ,  $6H$ ), C ( $1T$ ,  $2T$ ,  $3R$ ) and D ( $2H_1$ ,  $2H_2$ ,  $6R$ ), on the basis of the interlayer shift and of the rotation between succeeding layers (Bailey, 1969). In the Order-Disorder theory (Dornberger-Schiff and Āurovič, 1975) these polytypes are defined as *MDO* polytypes (Maximum Degree Order). Among them, only 8 polytypes have been reported for cronstedtite in the literature (Table 1):  $1T$ ,  $1M$ ,  $2H_1$ ,  $2H_2$ ,  $2M_1$ ,  $2T$ ,  $3T$  and  $6R$  (Steadman and Nuttall, 1963, 1964). One non-standard or non-MDO polytype has also been found by Fron del (1962) in a cronstedtite sample coming from the Cornucopia mine (Nye Country, Nevada) and it was indicated by the Ramsdell symbol  $9R$ .

68 In terrestrial environments, cronstedtite was found in sulfide veins as a low-temperature hydrothermal mineral, associated with siderite, pyrite, sphalerite and quartz (Fron del, 1962) and also in metamorphosed massive sulphide deposits (Lopez-Garcia *et al.*, 1992). In Australian banded iron-formations of lower metamorphic grade, Gole (1980 a, b) reported the coexistence of greenalite with another mineral that he identified as probable cronstedtite.

73 Cronstedtite occurs also in carbonaceous chondrites both in fine-grained rims and matrices as  
74 product of aqueous alteration on the parent body (Müller *et al.*, 1979; Barber, 1981; Burbine  
75 and Burns, 1994, Browning *et al.*, 1996; Lauretta *et al.*, 2000; Zega and Buseck, 2003;  
76 Miyahara *et al.*, 2008)

77 A few experimental works reported the formation of T-O Fe-rich minerals of the serpentine  
78 group. Odinite ( $R^{3+}$ ,  $R^{2+}$ ,  $\square$ )<sub>3</sub>(Si<sub>2-x</sub> Al<sub>x</sub>)O<sub>5</sub>(OH)<sub>4</sub> and hexagonal crystals of cronstedtite as run  
79 products of dioctahedral smectites-iron metal interactions at 80° C were reported by Lantenois  
80 (2003), Lantenois *et al.* (2005) and Lanson *et al.* (2012). Under similar experimental  
81 conditions, Fe-rich T-O phyllosilicates were described as “berthierine type” phases with  
82 general formula ( $R^{2+}$ ,  $R^{3+}$ ,  $\square$ )<sub>3</sub>(Si<sub>2-x</sub>, Al<sub>x</sub>)O<sub>5</sub>(OH)<sub>4</sub> (Brindley, 1982) or “Fe-rich 7 Å clays” or  
83 “serpentine-like minerals” (Wilson *et al.*, 2006; Perronnet *et al.*, 2007; Mosser-Ruck *et al.*,  
84 2010; Jodin-Caumon *et al.*, 2010; de Combarieu *et al.*, 2011; Jodin-Caumon *et al.*, 2012;  
85 Rivard *et al.*, 2013), sometimes close to the greenalite end-member (Pierron, 2011). The  
86 numerous designations of low temperature Fe-rich phyllosilicates found in literature were  
87 explained by the difficulty of their identification. They often appeared as highly disordered or  
88 nanocrystalline phases (Schlegel *et al.*, 2008) or as small crystal associated with Si-Al-Fe  
89 gels (Perronnet *et al.*, 2008), and they can coexist with other Fe-rich phases in experimental  
90 run products.

91

## 92 **MATERIALS AND METHODS**

### 93 *Starting material*

94 The starting clay rich rock used in our experiments is a claystone from the Callovo-Oxfordian  
95 formation (noted COx) of the Paris Basin, a formation investigated for future waste storage in  
96 the underground research laboratory (URL) at the Meuse/Haute-Marne site of Bure (France).

97 The claystone contains on average 41% of clay minerals (illite, mixed-layered illite/smectite,

98 being the predominant clay minerals, and minor amounts of kaolinite and chlorite), 25% of  
99 quartz, 31% of carbonates (calcite and minor dolomite) and the remaining 3% consist of  
100 pyrite, phosphates, K-feldspar and organic matter (Rousset, 2002; Gaucher *et al.*, 2004).  
101 The starting products (experimental solutions and clays) were prepared under inert argon  
102 atmosphere, using a solution of 0.0207 mol/kg NaCl and 0.0038 mol/kg CaCl<sub>2</sub> (pH = 6.4) and  
103 1 g of claystone grinded in a mortar to obtain a liquid/solid mass ratio of 10. Metal iron was  
104 added to the system as a powder (500 mg; average grain size ~ 40 μm) and as two plates with  
105 dimensions of nearly 3x6x1mm<sup>3</sup> (iron powder/CO<sub>x</sub> mass ratio of 0.5). The starting mixture  
106 was put in Parr® non-stirred pressure vessels made of Teflon® with capacity of ~20 ml.  
107 Seven vessels were heated in a furnace at 90(±2)° C for 6 months and then the temperature  
108 was decreased every month by steps of 10°C until 40°C. At each temperature, a vessel was  
109 removed from the oven. After quenching and opening of each vessel, the solid run products  
110 were dried under an argon flux at room temperature.

111

#### 112 *ManoCalcimeter*

113 Quantitative analysis of carbonates was performed in the Museum National d'Histoire  
114 Naturelle (MNHN) using a Mélières manoCalcimeter (MCM) on 200 mg of bulk rock sample  
115 powder (see Ledéseret *et al.*, 2009). MCM uses a “Karbonat-Bombe” which is a simple  
116 apparatus composed of glass flask and a high precision manometer (Dunn, 1980). This  
117 method gives a direct measurement of carbonates for rocks containing only calcite or  
118 aragonite (CaCO<sub>3</sub>). The MCM is built to give a 100 mg value when 1 millimole of CO<sub>2</sub> is  
119 emitted during chemical attack of 100 mg (# 1 millimole) of CaCO<sub>3</sub> by 8N hydrochloric acid.  
120 Nevertheless, molecular weight of carbonates varying with their chemical composition and  
121 100 mg of pure dolomite for example provokes the emission of 1.085 millimole of CO<sub>2</sub>. As a  
122 consequence, the values read on the MCM must be corrected as a function of the amount of

123 the different carbonates identified by XRD. Calibration was performed using pure calcite  
124 crystals; uncertainty precision is around 0.5 wt.%.

125

### 126 *X-ray diffraction*

127 The data were collected at room temperature with a D8 Bruker diffractometer, using the  
128 CoK $\alpha$  radiation ( $\lambda = 1.7902 \text{ \AA}$ ), 35kV accelerating voltage and 45mA intensity. The Bruker  
129 DIFFRAC<sup>plus</sup> package was used for the data acquisition and analysis.

130 XRD patterns of randomly oriented powder were obtained, using a scan step of  $0.035^\circ$  ( $2\theta$ ),  
131 exposure time of 3 seconds,  $2\theta_{\min} = 3^\circ$  and  $2\theta_{\max} = 54^\circ$ .

132

### 133 *Scanning electron microscopy (SEM)*

134 The secondary electron (SE) and backscattered electrons (BSE) images of the cronstedtite  
135 crystals were obtained with an accelerating voltage of 15 kV using a cold FEG Hitachi S-  
136 4800. The lateral resolution of FEG-SEM is about 1 nm for SE images. The crystals of  
137 cronstedtite analysed were collected on the iron plates, deposited on the carbon adhesive  
138 sticks and then carbon coated. Energy dispersive X-ray spectra (EDXS) were performed to  
139 identify the chemical elements present in crystals.

140

### 141 *Transmission electron microscopy (TEM) and Energy-dispersive X-ray (EDX) spectroscopy*

142 TEM images and EDX analyses were carried out at 200 kV using a Philips CM20 microscope  
143 with a point resolution of 0.27 nm equipped with Si-Li detector. The TEM specimens were  
144 prepared dispersing the  $< 2 \mu\text{m}$  fraction powders in ethanol under ultrasonic and evaporating a  
145 drop of the suspension on a carbon network-like holey support film placed on a 200 mesh  
146 copper grid (Euromedex-Mundolcheim, France). The chemical composition of run products  
147 was determined using energy dispersive X-Ray spectroscopy (EDXS). EDX spectra were

148 recorded by means of a PGT spectrometer mounted on CM20 Philips microscope operated at  
149 200 kV and equipped with an ultrathin window X-Ray detector. The analyses were carried out  
150 in nanoprobe mode with a probe diameter of 10 nm using  $K_{AB}$  determined from clay standards  
151 with similar thickness.

152 Selected area electron diffraction (SAED) patterns were recorded at 120 kV using a Philips  
153 CM120 microscope with a Digistar Nanomegas CCD camera.

154

#### 155 *Automated electron diffraction tomography (ADT)*

156 3D electron diffraction data were also collected by a Tecnai F30 S-Twin microscope  
157 operating at 300 kV. Powdered sample (< 2  $\mu\text{m}$  fraction) was dispersed in ethanol, sonified  
158 and sprayed on a carbon-coated copper grid by a UIS250v Hielscher sonifier, according to the  
159 procedure described by Mugnaioli *et al.* (2009). Data collection was carried out by a  
160 combination of automated diffraction tomography (ADT) and precession electron diffraction  
161 (PED) (Kolb *et al.*, 2007, 2008; Mugnaioli *et al.*, 2009). Nano electron diffraction patterns  
162 were collected in steps of  $1^\circ$  in a tilt range up to  $-60/+60^\circ$ . Data processing, 3D reciprocal  
163 space reconstruction and cell parameter determination were performed by ADT3D software.

164

#### 165 *Analysis of solutions*

166 The pH of each run solution was measured with a combination of silver/sulfide electrode in  
167 glove box after cooling at room temperature and 0.025  $\mu\text{m}$  filtration. The electrode was  
168 calibrated using reference buffer solutions certified by PTB and NIST Institutes with pH 4, 7  
169 and 10. The run solutions were diluted ten times in 2% vol.  $\text{HNO}_3$  and analyzed by  
170 inductively coupled plasma optical emission spectroscopy (ICP-OES) at LIMOS laboratory to  
171 determine the concentration of dissolved Si and Fe.

172

## RESULTS

173

### 174 *ManoCalcimeter and X-ray diffraction*

175 XRD patterns of untreated mixed iron-CO<sub>x</sub> sample and run samples are shown in Figure 1.  
176 Calcite reflection at 3.03 Å is unchanged on the 90°C to 40°C patterns, indicating that this  
177 mineral is unaffected by the cooling. As the manoCalcimeter results confirm that calcite  
178 content is constant (10±1 wt%) in all samples, XRD patterns were normalized to calcite  
179 reflection (3.03 Å). Intensities of quartz, iron metal and T-O-T phyllosilicates (mica and illite)  
180 reflections decrease on XRD pattern of 90°C experiment. This decrease is emphasized on the  
181 other XRD patterns corresponding to 80°C-40°C experiments. At the same time, intensities of  
182 magnetite and 7 Å phyllosilicates increase. This indicates a strong dissolution of quartz and  
183 iron metal (more than 70% for both phases) and partial destruction of T-O-T phyllosilicate  
184 layers. The XRD results highlight the increase of the 7 Å clays amount in run products but  
185 don not allow to accurately distinguish T-O minerals because of their similar  $d_{hkl}$  values.

186

### 187 *Scanning electron microscopy*

188 The SEM analyses show that dominant 7 Å clays obtained in the 90°C experiment are iron-  
189 rich and have different morphologies (Figure 2). Pyramidal (truncated or not) crystal with a  
190 triangular base and conic crystals were observed. The last ones have rounded or hexagonal  
191 cross-sections (Figure 2a-b). The different morphologies still coexist down to 70° C (Figure  
192 2c-d), then at lower temperatures pyramidal shape becomes the dominant morphology (Figure  
193 2e-f).

194

### 195 *Transmission electron microscopy*

### 196 *Energy dispersive X-ray analyses and TEM imaging*

197 EDX analyses were performed on isolated particles of < 2 μm fraction powders. From the  
198 EDX results, structural formulae have been calculated on the basis of 7 oxygens and the  
199 Fe<sup>3+</sup>/Fe<sup>2+</sup> ratio has been adjusted to set the occupation of the octahedral sites to 3. The  
200 compositions (expressed as a.p.f.u., *i.e.* atom per formula unit) of 28 pyramidal crystals and 5  
201 conic crystals formed at 90° and 80° C are reported in Tables 2 and 3. The mean formula is:



203 The difference in the chemistry of crystals with respect to their morphology is not significant  
204 considering the standard deviation (Tables 2 and 3). The Si-deficit and the presence of ferric  
205 iron in the tetrahedral sites allow to identify these two types of crystals as cronstedtite.

206 TEM images show that the higher crystallinity of the newly formed iron rich clays was  
207 observed in 70°C and 60°C run products (Figure 3) and also that this mineral becomes  
208 unstable at temperature ≤ 50°C as demonstrated by alteration of its faces (Figure 4). At 40°C  
209 very rare relict crystals of altered cronstedtite were still observed.

210

#### 211 *SAED patterns and ADT/PED investigations: determination of cronstedtite polytypes*

212 Because of their great abundance in run product, well-shaped pyramidal cronstedtites formed  
213 during 70°C experiment were chosen to identify their MDO polytypes following the  
214 procedure described by Āurovič (1981). According to the Order-Disorder (OD) theory  
215 (Dornberger-Schiff, 1956, 1964, 1966, and 1979), the superposition vectors and rotations (of  
216 almost identical 1:1 layers) needed to obtain the four possible subfamily structures, are as  
217 follows: ±**a**<sub>i</sub>/3 for subfamily A; ±**b**/3 or zero for subfamily C; ±**a**<sub>i</sub>/3, and ±**b**/3 or zero  
218 combined with 180° rotation for subfamilies B and D, respectively (Dornberger-Schiff, 1964;  
219 Bailey, 1969). The **a**<sub>i</sub> and **b** are hexagonal and orthohexagonal unit cell vectors, respectively.

220 It follows that the subfamily sublattice corresponding to the Fourier transform of subfamily  
221 structure is formed by reflections with  $k = 3n$  (in orthohexagonal indexing, or  $h-k = 3n$  in

222 hexagonal indexing). These reflections are common to all polytypes belonging to the same  
223 subfamily and are consequently called *subfamily reflections*. Whereas the reflection having  $k$   
224  $\neq 3n$  (in orthohexagonal indexing, or  $h-k \neq 3n$  in hexagonal indexing) are typical of each  
225 polytypes and are said *non-family* or *polytype reflections*. Usually diffraction patterns of two  
226 orthogonal reciprocal lattice sections are enough to identify a MDO polytype: the diffraction  
227 pattern of  $(h0l)^*$  ( $hhl$  in hexagonal indexing) containing the subfamily reflections allowing to  
228 determine the subfamily and the diffraction pattern from  $(0kl)^*$  ( $\bar{h}hl$  in hexagonal indexing),  
229 containing both subfamily and polytype reflection useful to identify the polytype (Ďurovič,  
230 1997). In non-trigonal and non-hexagonal polytypes, however, the diffraction pattern of the  
231  $(0kl)^*$  plane is different from that of  $(h0l)^*$ , because they are not symmetry equivalent  
232 (Ďurovič, priv. comm.). In order to determine such polytypes to a certainty the  $(0kl)^*$  planes  
233 should be recorded and checked as well.

234 The spots distribution on experimental electron diffraction 2D patterns were compared with  
235 the identification diagrams for MDO polytypes of cronstedtite described in literature  
236 (Ďurovič, 1997, Hybler *et al.*, 2008), and with diffraction patterns theoretically calculated  
237 with aid of the DIFK91 program (Smrčok and Weiss, 1993).

238 SAED patterns of several pyramidal cronstedtites underline that they are all  $1M$  polytypes.  
239 The spot distribution along the  $11l$  reciprocal lattice row on  $(hhl_{\text{hex}})^*$  plane indicates that these  
240 crystals belong to the subfamily (Bailey's group) A (Figure 5). Moreover the spot distribution  
241 on  $(h0l_{\text{hex}})^*$  and  $(0kl_{\text{hex}})^*$  planes corresponds to MDO group II and I respectively (Figure 6).  
242 Both are in agreement with theoretically calculated patterns.  $1M$  cronstedtite polytype is very  
243 rare and generally occurs intergrown to the  $3T$  polytype and strongly disordered (Ďurovič,  
244 1997).

245 Three ADT data sets were collected on different crystals and reconstructed in 3D diffraction  
246 volumes. The first acquisition, coming from a nicely shaped pyramidal crystal (Figure 7a),

247 shows diffuse scattering along  $c^*$  for both  $h0l_{\text{hex}}$  and  $hhl_{\text{hex}}$  reflections, so that no polytypic  
248 identification can be made (Figure 7b).

249 The second acquisition comes from a crystal with pyramidal shape, where two corners are  
250 truncated and one not (Figure 8a). Remarkably the not-truncated corner is characterized by  
251 diffuse disorder, while the rest of the crystal delivers a mostly coherent diffraction consistent  
252 with the subfamily A and to MDO group III, *i.e.*  $2M_1$  polytype (Figure 8b-d). The cell is  $C$ -  
253 centred monoclinic with parameters  $a = 5.5 \text{ \AA}$ ,  $b = 9.6 \text{ \AA}$ ,  $c = 14.4 \text{ \AA}$ ,  $\beta = 97.4^\circ$ . Systematic  
254 absences for reflections  $h0l$  with  $l \neq 2n$  suggest the presence of a glide plane  $c$  perpendicular  
255 to the  $b$  axis. This is in agreement with the space group  $Cc$  found by Steadman and Nuttall  
256 (1964) for this polytype. Worth noting is that  $2M_1$  polytype of cronstedtite is also very rare in  
257 nature (Đurovič, 1997). The presence of diffuse scattering along  $c^*$  testifies anyway to a  
258 certain degree of disorder even in most ordered parts of the crystal.

259 The third acquisition highlights the presence of another polytype belonging to the subfamily  
260 A and MDO group IV, *i.e.*  $3T$  polytype (Figure 9a-b). The cell is hexagonal with parameters  $a$   
261  $= 5.5 \text{ \AA}$ , and  $c = 21.4 \text{ \AA}$ . Intensity distribution suggests a trigonal symmetry (Laue class  $\bar{P}3$   
262 or  $\bar{P}31m$ ), consistent with the space group  $P3_1$  reported in literature (Steadman and Nuttall,  
263 1963; Smrčok *et al.*, 1994).

264

### 265 *Solution chemistry*

266 The characterization of run solutions shows that the mean pH value is  $7.47 \pm 0.16$  and that Si  
267 concentration varies between 7 and 11 ppm in function of the experiments (Figure 10). Quartz  
268 solubility at each run temperature has been calculated by PHREEQC geochemical software  
269 package V2.17 (Parkhurst and Appelo, 1999) and the associated LLNL database (Johnson *et*  
270 *al.*, 2000). Si concentration is under the quartz solubility curve in run solution of experiment  
271 carried out in the temperature range of  $90^\circ$ - $60^\circ$  C, whereas at  $50^\circ$  C the Si concentration is on

272 the quartz solubility curve. Finally, the Si concentration slightly increases in the last run  
273 solution (40° C). Fe concentration in the experimental solutions is very low (< 1 ppm) or  
274 under limit detection.

275

## 276 **DISCUSSION AND CONCLUSIONS**

277 The significant decrease of quartz, T-O-T phyllosilicates and iron metal intensity reflections  
278 on X-ray diffraction patterns indicates that these phases were dissolved releasing Si and Fe in  
279 experimental solutions. Quartz dissolution is confirmed by Si concentration measured in run  
280 solutions which is lower than that at equilibrium with quartz between 90°-60°C (Figure 10).  
281 At this temperature range, cronstedtite is formed together with other 7 Å clays. As iron  
282 content in run solutions is lower than 1 ppm or under limit of detection (< 5 ppb), it is all  
283 incorporated in newly formed minerals (cronstedtite, magnetite and other iron-rich silicates).  
284 At temperatures of 50° and 40°C measured Si content is respectively equal and higher than  
285 that at equilibrium with quartz, preventing the precipitation of cronstedtite. Thanks to the  
286 original step by step cooling procedure presented in this paper, the stability range of  
287 cronstedtite with respect to the temperature was determined. Between 90°C to 60°C  
288 cronstedtite appears to be stable and 50°C corresponds to the lower limit of cronstedtite  
289 stability as confirmed by crystal alteration (Results §). The upper limit is  $\geq 90^\circ\text{C}$  but it cannot  
290 be accurately determined. Surely, no cronstedtite has ever been observed in similar  
291 experiments carried out on the same claystone (COx) at higher temperatures of 150°C and  
292 300°C (Pierron, 2011).

293 The cooling experiments from 90°C to 60°C favored the development of crystals with  
294 pyramidal (truncated or not) morphologies and enhanced crystallinity. Pyramidal crystals  
295 analyzed by TEM show different polytypic sequences and various degrees of disorder. The  
296 identified polytypes, all belonging to the subfamily A, are  $2M_1$  and  $1M$  together with  $3T$ .

297 According to Hybler *et al.* (2008), these two monoclinic polytypes are very rare whereas 3*T*  
298 polytype is relatively abundant in nature. The mean formula for pyramidal polytypes is in  
299 good agreement with that reported by Kogure *et al.* (2002) for cronstedtite of subfamily A,  
300 even if our crystals contain small amounts of Al and Mg (Table 2). Conic crystals of  
301 cronstedtite occur with pyramidal ones only in 90°C and 80°C experiments. The coexistence  
302 of these two different morphologies may be due to changes of the supersaturation degree  
303 during growth. When the supersaturation decreased, the crystals take a polyhedral habitus  
304 bounded by flat faces (Sunagawa, 2005), changing the morphology from conic to pyramidal.  
305 According to the literature, one can also suppose that conic crystals may be cronstedtite  
306 polytypes belonging to the C or D subfamilies (Frondel, 1962; Kogure *et al.*, 2001; Hybler *et*  
307 *al.*, 2002). The co-occurrence of one of these two subfamilies with the subfamily A has been  
308 already observed (C + A or D + A subfamilies) by Hybler *et al.* (2008). The detailed study of  
309 conic crystals is the object of an investigation under development and will be discussed in a  
310 future work.

311

#### 312 *Comparison with cronstedtite from chondrites*

313 Several studies about the formation conditions of cronstedtite were carried out on  
314 carbonaceous chondrites in which this mineral is the dominant component (Dyl *et al.*, 2010).  
315 Cronstedtite crystals in meteorites are often small, platy and characterized by high degree of  
316 stacking disorder (Müller *et al.*, 1979; Lauretta *et al.*, 2000; Zega and Buseck., 2003). For this  
317 reason it is difficult to identify their polytypes. Nevertheless, Müller *et al.* (1979) and Zaga  
318 and Buseck (2003) found mostly 1*T* polytype and Müller *et al.* (1979) reported that the  
319 second more frequent polytype is 1*M*. Even if the conditions of cronstedtite formation in  
320 meteorites are close to those of our experiments (presence of metal Fe, neutral-alkaline  
321 solution, reducing conditions), 1*T* polytype was not observed in our run products. Mass-

322 transfer and reaction-path calculations simulating aqueous alteration in chondrites propose  
323 that the upper limit of cronstedtite stability is 90°-100°C according to Schulte and Shock  
324 (2004) and McAlister and Kettler (2008). These calculations were done with the hypothesis  
325 that the activity of silica in solution is close to quartz saturation. This disagrees with our  
326 chemical data obtained on experimental solution which indicate that the activity of aqueous  
327 silica is under quartz saturation between 90°C and 70°C.

328

### 329 *Comparison with run products in similar experimental conditions*

330 The results presented in this paper have shown that the occurrence of cronstedtite is restricted  
331 to the 90°C-50°C domain of temperature. But at 90°C, in the 6 months experiment,  
332 cronstedtite is not so abundant and its crystallinity degree is low. Is it a kinetic or temperature  
333 effect? To answer this question, our results were compared to those of similar experiments  
334 carried out on the same starting materials. Rivard (2011) and Pierron (2011) used the same  
335 claystone (COx of the Meuse/Haute-Marne site of Bure) at 90°C for 9 months but using  
336 slightly different liquid/solid mass ratio (20 and 10 respectively) and iron powder/COx mass  
337 ratio (0.2 and 0.1 or 1 respectively). They observed the crystallization of iron-rich T-O clays  
338 with a composition between odinite, berthierine and greenalite (Figure 11). No cronstedtite  
339 have been reported by these authors. These results seem to confirm that the formation of  
340 cronstedtite is strongly favored by a lower temperature range, and maybe by a temperature  
341 decrease.

342

### 343 *Concluding remarks*

344 In clay formations which may be host deep-geological radioactive waste disposal, a first  
345 increase of temperature to 90° C close to the containers and then followed by a cooling is  
346 expected. Our experiments simulated the mineralogical evolution of the iron-clay system

347 around the steel containers during a cooling between 90° and 40° C. They showed that the  
348 composition of iron rich T-O clays stable at 90°C (close to odinite, greenalite or berthierine)  
349 will evolve toward cronstedtite during the cooling. This result has to be taken into account in  
350 the understanding of complex interaction in glass-iron-clay systems.

351

## 352 ACKNOWLEDGMENTS

353 The authors thank L. Mouton and J. Ghanbaja respectively for SEM and TEM images and  
354 analyses at SCMEM laboratory (Université de Lorraine, France). U. Kolb is warmly thanked  
355 for providing access to TEM laboratory at the Institut für Physikalische Chemie, Johannes  
356 Gutenberg Universität. The authors also wish to thank M. Klementova and L. Palatinus for  
357 acquisition and processing of SAED patterns, L. Truche for helpful discussion. This research  
358 was financially supported by ANDRA – Agence Nationale pour la gestion des Déchets  
359 Radioactifs (French national agency for the management of radioactive wastes).

360

## 361 REFERENCES

- 362 Bailey, S.W. (1969) Polytypism of trioctahedral 1:1 layer silicates. *Clays and Clay Minerals*,  
363 **17**, 355-371.
- 364 Bailey, S.W. (1988) Odinite, a new dioctahedral-trioctahedral Fe<sup>3+</sup>-rich 1:1 clay mineral. *Clay*  
365 *Minerals*, **23**, 237-247.
- 366 Barber, D.J. (1981) Matrix phyllosilicates and associated minerals in C2M carbonaceous  
367 chondrites. *Geochimica et Cosmochimica Acta*, **45**, 945-970.
- 368 Brindley, G.W. (1982) Chemical compositions of berthierines – A review. *Clays and Clay*  
369 *Minerals*, **30**, 153-155.

370 Browning, L.B., McSween, H.Y. Jr. and Zolensky, M.E. (1996) Correlated alteration effects  
371 in CM carbonaceous chondrites. *Geochimica et Cosmochimica Acta*, **60**, 2621-2633.

372 Burbine, T.H. and Burns, R.G. (1994) Questions concerning the oxidation of the ferrous iron  
373 in carbonaceous chondrites. *Lunar Planetary Science*, **XXV**, 199-200.

374 de Combarieu, G., Schlegel, M.L., Neff, D., Foy, E. Vantelon, D., Barboux, P. and Gin, S.  
375 (2011) Glass-iron-clay interactions in a radioactive waste geological disposal : an  
376 integrated laboratory-scale experiment. *Applied Geochemistry*, **26**, 65-79.

377 Dornberger-Schiff, K. (1956) On Order-Disorder Structures (OD-Structures). *Acta*  
378 *Crystallographica*, **9**, 593-601.

379 Dornberger-Schiff, K. (1964) Grundzüge einer Theorie von OD-Strukturen aus Schichten.  
380 Abh. dtsh. Akad Wiss Berlin, Kl. f. Chem., 3, 107 p.

381 Dornberger-Schiff, K. (1966) Lehrgang über OD-Strukturen. Berlin: Akademie-Verlag, 135  
382 p.

383 Dornberger-Schiff, K. (1979) OD structures- a game and a bit more. *Kristall Und Technik*, **14**,  
384 1027-1045.

385 Dornberger-Schiff, K. and Ďurovič, S. (1975) OD-interpretation of kaolinite-type structure-I:  
386 symmetry of kaolinite packets and their stacking possibilities. *Clays and Clay Minerals*,  
387 **23**, 219-229.

388 Dunn, D.A. (1980). Revised techniques for quantitative calcium carbonate analysis using the  
389 "Karbonat-Bombe," and comparisons to other quantitative carbonate analysis methods.  
390 *Journal of Sedimentary Research*, **50**, 631-636.

391 Ďurovič, S. (1981) OD-Charakter, Polytypie und Identifikation von Schichtsilikaten.  
392 *Fortschritte der Mineralogie*, **59**, 191-226.

393 Ďurovič, S. (1997) Cronstedtite-1M and co-existence of 1M and 3T polytypes. *Ceramics –*  
394 *Silikáty*, **41** (3), 98-104.

395 Dyl, K.A., Manning, C.E. and Young, E.D. (2010) The implication of the cronstedite in  
396 water-rich planetesimals and asteroids. Astrobiology Science Conference 2010, League  
397 City, Texas.

398 Frondel, C. (1962) Polytypism in cronstedtite. *American Mineralogist*, **47**, 781-783.

399 Gaucher, E., Robelin, C., Matray, J.M., Négrel, G., Gros, Y., Heitz, J.F., Vinsot, A., Rebours,  
400 H., Cassagnabère, A. and Bouchet, A. (2004) ANDRA underground research laboratory :  
401 interpretation of the mineralogical and geochemical data acquired in the Callovian-  
402 Oxfordian formation by investigative drilling. *Physics and Chemistry of the Earth*, **29**,  
403 55-77.

404 Geiger, C.A., Henry, D.L., Bailey, S.W. and Maj, J.J. (1983) Crystal structure of cronstedtite-  
405  $2H_2$ . *Clays and Clay Minerals*, **31**, 97-108.

406 Gole, M.J. (1980a) Low-temperature retrograde minerals in metamorphosed Archean banded  
407 iron-formations, Western Australia. *Canadian Mineralogist*, **18**, 205-214.

408 Gole, M.J. (1980b) Mineralogy and petrology of very-low metamorphic grade Archean  
409 banded iron-formations, Weld Range, Western Australia. *American Mineralogist*, **65**, 8-  
410 25.

411 Guggenheim, S., Bailey, S.W., Eggleton, R.A. and Wilkes, P. (1982) Structural aspects of  
412 greenalite and related minerals. *Canadian Mineralogist*, **20**, 1-18.

413 Hendricks, S.B. (1939) Random Structures of layer minerals as illustrated by cronstedtite  
414 ( $2FeO \cdot Fe_2O_3 \cdot SiO_2 \cdot 2H_2O$ ). Possible iron content of kaolin. *American Mineralogist*, **24**,  
415 529-539.

416 Hybler, J., Ďurovič, S. and Kogure, T. (2008) Polytypism in cronstedtite. *Acta*  
417 *Crystallographica*, **A64**, C498-499.

418 Hybler, J., Petříček, V., Ďurovič, S. and Smrčok, L. (2000) Refinement of the crystal structure  
419 of cronstedtite-1T. *Clays and Clay Minerals*, **48**, 331-338.

420 Hybler, J., Petříček, V., Fábry, J. and Ďurovič, S. (2002) Refinement of the crystal structure  
421 of cronstedtite- $2H_2$ . *Clays and Clay Minerals*, **50**, 601-613.

422 Jodin-Caumon, M.C., Mosser-Ruck, R., Randi, A., Pierron, O., Cathelineau, M. and Michau,  
423 N. (2012) Mineralogical evolutions of a claystone after reaction with iron under thermal  
424 gradient. *Clays and Clay Minerals*, **60**, 5, 443-455.

425 Jodin-Caumon, M.C., Mosser-Ruck, R., Rousset, D., Randi, A., Cathelineau, M. and Michau,  
426 N. (2010) Effect of a thermal gradient on iron-clay interactions. *Clays and Clay Minerals*,  
427 **58**, 5, 667–681.

428 Johnson, L., Anderson, G., Parkhurst, D. (2000) Database from ‘thermo.com.V8.R6.230’  
429 Prepared at Lawrence Livermore National Laboratory (Revision: 1.11).

430 Kogure, T., Hybler, J. and Ďurovič, S. (2001) A HRTEM study of cronstedtite : determination  
431 of polytypes and layer polarity in trioctahedral 1 :1 phyllosilicates. *Clays and Clay*  
432 *Minerals*, **49**, 310-317.

433 Kogure, T., Hybler, J. and Yoshida, H. (2002) Coexistence of two polytypic groups in  
434 cronstedtite from Lostwithiel England. *Clays and Clay Minerals*, **50**, 504-513.

435 Kolb, U., Gorelik, T. and Otten, M.T. (2008) Towards automated diffraction tomography.  
436 Part II – Cell parameter determination. *Ultramicroscopy*, 108, 763-772.

437 Kolb, U., Gorelik, T., Kübel, C. and Otten, M.T. (2007) Towards automated diffraction  
438 tomography : Part I – Data acquisition. *Ultramicroscopy*, **107**, 507-513.

439 Lanson, B., Lantenois, S. Van Aken, P.A., Bauer, A. and Plançon, A. (2012) Experimental  
440 investigation of smectite interaction with metal iron at 80°C : structural characterization  
441 of newly formed Fe-rich phyllosilicates. *American Mineralogist*, **97**, 864-871.

442 Lantenois, S. (2003) Réactivité fer metal/smectites en milieu hydraté à 80°C, Ph.D. thesis,  
443 Université d’Orleans, Orleans, 220 pp.

444 Lantenois, S., Lanson, B., Muller, F., Bauer, A., Jullien, M. and Plançon, A. (2005)  
445 Experimental study of smectite interaction with metal Fe at low temperature: 1. Smectite  
446 destabilization. *Clays and Clay Minerals*, **53**, 597-612.

447 Lauretta, D.S., Hua, X. and Buseck, P.R. (2000) Mineralogy of fine-grained rims in the ALH  
448 81002 CM chondrite. *Geochimica et Cosmochimica Acta*, **64**, 3263-3273.

449 Ledéser B., Hébert R., Grall C., Genter A., Dezayes C., Bartier D. and Gérard A. (2009).  
450 Calcimetry as a useful tool for a better knowledge of flow pathways in the Soultz-sous-  
451 Forêts Enhanced Geothermal System, *Journal of Volcanology and Geothermal Research*,  
452 **181**, 106-114.

453 López García, J.A., Manteca, J.I., Prieto, A.C. and Calvo, B. (1992) Primera aparición en  
454 España de cronstedtita. Caracterización estructural. *Boletín de la Sociedad Española de*  
455 *Mineralogía*, **15-1**, 21-25.

456 McAlister, J.A. and Kettler, R.M. (2008) Metastable equilibria among dicarboxylic acids and  
457 the oxidation state during aqueous alteration on the CM2 chondrite parent body.  
458 *Geochimica et Cosmochimica Acta*, **72**, 233-241.

459 Miyahara, M., Uehara, S., Ohtani, E., Nagase T., Nishijima, M., Vashaei, Z. and Kitagawa, R.  
460 (2008) The anatomy of altered chondrules and FGRs covering hem in a CM chondrite by  
461 FIB-TEM-STEM. *Lunar Planetary Science*, **XXXIX**, 199-200.

462 Mosser-Ruck, R., Cathelineau, M., Guillaume, D. and Charpentier, D. (2010) Effects of  
463 temperature, pH, and iron/clay and liquid/clay ratios on experimental  
464 conversion of dioctahedral smectite to berthierine, chlorite, vermiculite, or saponite.  
465 *Clays and Clay Minerals*, **58**, 280-291.

466 Mugnaioli, E., Gorelik, T. and Kolb, U. (2009) “Ab initio” structure solution from electron  
467 diffraction data obtained by a combination of automated diffraction tomography and  
468 precession technique. *Ultramicroscopy*, **109**, 758-765.

469 Müller, W.F., Kurat, G. and Kracher, A. (1979) Chemical and crystallographic study of  
470 cronstedtite in the matrix of the Cochabamba (CM2) carbonaceous chondrite. *Tschermaks*  
471 *Mineralogische und Petrographische Mitteilungen*, **26**, 293-304.

472 Parkhurst, D.L., Appelo, C.A.J. (1999) User's guide to PHREEQC (Version 2). A Computer  
473 Program for Speciation, Batch-reaction, One-dimensional Transport, and Inverse  
474 Geochemical Calculations. U.S. Geological Survey Water-Resources Investigations  
475 Report 99-4259, 312 pp.

476 Perronnet, M., Jullien, M., Villiéras, F., Raynal, J., Bonnin, D. and Bruno, G. (2008) Evidence  
477 of a critical content in Fe(0) on FoCa7 bentonite reactivity at 80°C. *Applied Clay Science*,  
478 **38**, 187-202.

479 Perronnet, M., Villiéras, F., Jullien, M., Razafitianamaharavo, A., Raynal, J. and Bonnin, D.  
480 (2007) Towards a link between the energetic heterogeneities of the edge of smectites and  
481 their stability in the context of metallic corrosion. *Geochimica et Cosmochimica Acta*, **71**,  
482 1463-1479.

483 Pierron, O. (2011) Interactions eau-fer-argilite : rôle des paramètres Liquide/Roche,  
484 Fer/Argilite, Température sur la nature des phases minérales, Ph.D. thesis, Université  
485 Henri Poincaré, Nancy, 226 pp.

486 Rivard, C. (2011) Contribution à l'étude de la stabilité des minéraux constitutifs de l'argilite  
487 du Callovo-Oxfordien en présence de fer à 90°C, Ph.D. thesis, Institut National  
488 Polytechnique de Lorraine, Nancy, 338 pp.

489 Rivard, C., Pelletier, M., Michau, N., Razafitianamaharavo, A., Bihannic, I., Abdelmoula, M.,  
490 Ghanbaja, J. and Villiéras, F. (2013) Berthierine-like mineral formation and stability  
491 during the interaction of kaolinite with metallic iron at 90 °C under anoxic and oxic  
492 conditions. *American Mineralogist*, **98**, 163-180.

493 Rousset, D. (2002) Etude de la fraction argileuse de séquence sédimentaires de la Meuse et du  
494 Gard. Reconstruction de l'histoire diagénétique et des caractéristiques physico-chimiques  
495 des cibles, Ph.D. thesis, Université Louis Pasteur, Strasbourg, 269 pp.

496 Schlegel, M.L., Bataillon, C., Benhamida, K., Blanc, C., Menut, D. and Lacour, J. (2008)  
497 Metal corrosion and argillite transformation at the water-saturated, high-temperature iron-  
498 clay interface : a microscopic-scale study. *Applied Geochemistry*, **23**, 2619-2633.

499 Schulte, M. and Schock, E. (2004) Coupled organic synthesis and mineral alteration on the  
500 meteorite parent bodies. *Meteoritic and Planetary Science*, **39**, 1577-1590.

501 Smrčok, L., Ďurovič, S., Petříček, V. and Weiss, Z. (1994) Refinement of the crystal structure  
502 of cronstedtite-3T. *Clays and Clay Minerals*, **42**, 544-551.

503 Smrčok, L., Weiss, Z (1993) DIFK91: a program for the modelling of powder diffraction  
504 patterns on a PC. *Journal of Applied Crystallography* 26, 140-141.

505 Steadman, R. and Nuttall, P.M. (1963) Polymorphism in cronstedtite. *Acta Crystallographica*,  
506 **16**, 1-8.

507 Steadman, R. and Nuttall, P.M. (1964) Further polymorphism in cronstedtite. *Acta*  
508 *Crystallographica*, **17**, 404-406.

509 Sunagawa, I. (2005) *Crystals. Growth, morphology and perfection*, Cambridge University  
510 Press.

511 Wilson, J., Cressey G., Cressey, B., Cuadros, J., Vala Ragnarsdottir, K., Savage, D. and  
512 Shibata, M. (2006) The effect of iron on montmorillonite stability. (II) Experimental  
513 investigation. *Geochimica et Cosmochimica Acta*, **70**, 323-336.

514 Zega, T.J. and Buseck, P.R. (2003) Fine-grained-rim mineralogy of the Cold Bokkeveld CM  
515 chondrite. *Geochimica et Cosmochimica Acta*, **67**, 1711-1721.

516

517

518

## TABLES

519 **Table 1.** Polytypes of trioctahedral T-O phyllosilicates and cronstedtite (literature data).

520

521 **Table 2.** Cation contents (a.p.f.u, *i.e.* atom per formula unit) in 28 pyramidal crystals of  
522 cronstedtite formed between 90° and 80°C.

523

524 **Table 3.** Cation contents (a.p.f.u) in 5 conic crystals of cronstedtite formed between 90° and  
525 80°C.

526

527

## FIGURES CAPTIONS

528 **Figure 1.** XRD patterns of run samples collected from 90°C to 40°C experiments and  
529 untreated mixed iron-CO<sub>x</sub> sample (Chl = chlorite, T-O-T Ph = T-O-T phyllosilicates, Qz =  
530 quartz).

531

532 **Figure 2.** a) SEM image of cronstedtite crystals with different morphologies in 90°C  
533 experiment and a relative EDX spectrum (b). c), d) BSE images of conic (in circle) and  
534 pyramidal cronstedtites in 70°C experiment. e), f) BSE and SE images of pyramidal crystals  
535 of cronstedtite in 60°C experiments.

536

537 **Figure 3.** TEM micrographs of conic (a, b) and pyramidal cronstedtites (c, d) formed between  
538 90° and 80°C.

539

540 **Figure 4.** TEM image of unstable cronstedtite crystal in 50°C experiment.

541

542 **Figure 5.** SAED pattern of  $(hhl_{\text{hex}})^*$  plane for  $1M$  polytype. Note, that the pattern contains  
543 also few weak parasitic spots of an unidentified phase.

544

545 **Figure 6.** SAED patterns of  $(h0l_{\text{hex}})^*$  and  $(0kl_{\text{hex}})^*$  planes for  $1M$  polytype.

546

547 **Figure 7.** First ADT acquisition. a) TEM image of the pyramidal crystal selected for ADT  
548 acquisition. b) ADT 3D diffraction reconstruction (along an oblique view) showing the  
549 diffuse scattering along  $c^*$ .

550

551 **Figure 8.** Second ADT acquisition. a) TEM image of the truncated crystal. The area pointed  
552 by the black arrow was affected by diffuse disorder, while the area pointed by the white arrow  
553 was selected for ADT acquisition. b) ADT 3D diffraction reconstruction viewed along  $a^*$ .  
554 White arrows point the reflections  $h0l$  with  $l \neq 2n$  extinct due the  $c$ -glide plane. c) ADT 3D  
555 diffraction reconstruction viewed along  $b^*$ . d) ADT 3D diffraction reconstruction viewed  
556 along  $c^*$ . An extraneous reflection coming from another crystal is marked with a circle. Note  
557 that these are projections of a 3D diffraction volume and not conventional 2D electron  
558 diffraction patterns.

559

560 **Figure 9.** Third ADT acquisition. a) TEM image of the crystal selected for the acquisition  
561 (indicated by a black arrow). b) ADT 3D diffraction reconstruction viewed along  $a^*$  showing  
562 the 21.4 Å periodicity.

563

564 **Figure 10.** Si concentration (ppm) in run solutions vs experimental temperature.

565

566 **Figure 11.** Chemical composition of the most evolved newly formed T-O clays plotted in a  
567 Si-Al-Fe<sub>TOT</sub> ternary diagram. Experiments of this study are represented by diamonds.  
568 Pierron's experiments (2011) and Rivard's experiments (2011) are represented respectively  
569 by squares and triangles. Gr: greenalite (Fe<sup>3+</sup><sub>0.45</sub>Fe<sup>2+</sup><sub>1.9</sub>Mg<sub>0.3</sub>□<sub>0.35</sub>)Si<sub>2.0</sub>O<sub>5</sub>(OH)<sub>4</sub> (Guggenheim  
570 *et al.*, 1982); Od: odinite (Al<sub>0.15</sub>Fe<sup>3+</sup><sub>1.2</sub>Fe<sup>2+</sup><sub>0.35</sub>Mg<sub>0.7</sub>□<sub>0.6</sub>)(Si<sub>1.85</sub>Al<sub>0.15</sub>)O<sub>5</sub>(OH)<sub>4</sub> (Bailey, 1988);  
571 Be: berthierine (Al<sub>0.96</sub>Fe<sup>3+</sup><sub>0.22</sub>Fe<sup>2+</sup><sub>1.49</sub>Mg<sub>0.17</sub>□<sub>0.17</sub>)(Si<sub>1.15</sub>Al<sub>0.85</sub>)O<sub>5</sub>(OH)<sub>4</sub> (Brindley, 1982); Cr:  
572 cronstedtite (Fe<sup>3+</sup><sub>0.84</sub>Fe<sup>2+</sup><sub>2.16</sub>)(Si<sub>1.16</sub>Fe<sup>3+</sup><sub>0.84</sub>)O<sub>5</sub>(OH)<sub>4</sub> (Kogure *et al.*, 2002).

573

574

**Table 1**

Polytypes of trioctahedral T-O phyllosilicates	<b><i>MDO polytypes of trioctahedral T-O phyllosilicates</i></b>				Authors
	A	B	C	D	Bailey (1969)
	<i>1M, 2M<sub>1</sub>, 3T</i>	<i>2O, 2M<sub>2</sub>, 6H</i>	<i>1T, 2T, 3R</i>	<i>2H<sub>1</sub>, 2H<sub>2</sub>, 6R</i>	
	<b><i>MDO polytypes of cronstedtites</i></b>				
	<i>1M, 2M<sub>1</sub>, 3T</i>		<i>1T, 2T</i>	<i>2H<sub>1</sub>, 2H<sub>2</sub>, 6R</i>	Steadman and Nuttall, (1963, 1964)
Most frequent morphologies	Truncated trigonal pyramid shape, plates needles ( <i>3T</i> )		Cones or trigonally deformed cones ( <i>1T</i> )	Ovoid based shape or columnar with rounded hexagonal or circular cross section (group D). Ovoid-to barrel-shaped morphology ( <i>2H<sub>2</sub></i> )	Frondel, (1962); Hybler et al. (2000; 2002); Steadman and Nuttall, (1963); Kogure et al., (2001); Geiger et al. (1983)
Polytypes of trioctahedral T-O phyllosilicates	<b>Non-MDO polytypes of cronstedtites : 9R</b> Cornucopia mine (Nye Country, Nevada)				Frondel (1962)

575

576

Table 2

	<b>Mg</b>	<b>Fe<sub>tot</sub></b>	<b><sup>IV</sup>Al</b>	<b>Si</b>	<b><sup>IV</sup>Fe</b>	<b><sup>VI</sup>Fe<sup>2+</sup></b>	<b><sup>VI</sup>Fe<sup>3+</sup></b>
	0	3.79	0.02	1.19	0.79	2.18	0.81
	0.03	3.73	0.06	1.18	0.76	2.15	0.82
	0.02	3.68	0.09	1.20	0.70	2.18	0.80
	0	3.27	0.02	1.71	0.27	2.71	0.29
	0.10	3.54	0.19	1.17	0.64	2.07	0.83
	0.14	3.37	0.20	1.28	0.52	2.14	0.72
	0.03	3.71	0.11	1.15	0.74	2.12	0.88
	0.01	3.85	0.06	1.08	0.86	2.07	0.92
	0.01	3.73	0.04	1.22	0.74	2.21	0.78
	0.02	3.71	0.03	1.24	0.73	2.23	0.76
	0.01	3.81	0.02	1.16	0.82	2.15	0.84
	0	3.73	0.08	1.19	0.73	2.19	0.81
	0	3.89	0	1.11	0.89	2.11	0.89
	0.03	3.80	0.03	1.14	0.83	2.10	0.86
	0.07	3.35	0.27	1.31	0.42	2.24	0.70
	0	3.61	0.08	1.30	0.61	2.30	0.70
	0	3.84	0	1.16	0.84	2.16	0.84
	0.03	3.91	0.03	1.04	0.93	2.01	0.96
	0.06	3.59	0.10	1.25	0.65	2.19	0.75
	0	3.86	0	1.14	0.86	2.14	0.86
	0.04	3.89	0.03	1.04	0.93	2.00	0.96
	0.01	3.70	0.07	1.22	0.71	2.21	0.78
	0.02	3.82	0.07	1.10	0.84	2.08	0.90
	0.01	3.71	0.06	1.22	0.72	2.21	0.78
	0	3.77	0	1.23	0.77	2.23	0.77
	0	3.88	0	1.12	0.88	2.12	0.88
	0.01	3.76	0.05	1.18	0.77	2.18	0.82
	0.01	3.81	0.09	1.10	0.81	2.09	0.90
	0.06	3.27	0.28	1.38	0.33	2.32	0.61
Average	0.03	3.70	0.07	1.20	0.73	2.17	0.80
$\sigma$	0.03	0.18	0.08	0.13	0.16	0.13	0.13

578

579

Table 3

	<b>Mg</b>	<b>Fe<sub>tot</sub></b>	<b><sup>IV</sup>Al</b>	<b>Si</b>	<b><sup>IV</sup>Fe</b>	<b><sup>VI</sup>Fe<sup>2+</sup></b>	<b><sup>VI</sup>Fe<sup>3+</sup></b>
	0.01	3.74	0.07	1.18	0.75	2.17	0.82
	0.04	3.60	0.14	1.22	0.64	2.18	0.78
	0.04	3.59	0.15	1.21	0.63	2.17	0.79
	0.01	3.75	0.10	1.14	0.76	2.13	0.86
	0.04	3.53	0.26	1.17	0.58	2.12	0.84
Average	0.03	3.64	0.14	1.18	0.67	2.16	0.82
$\sigma$	0.02	0.10	0.07	0.03	0.08	0.03	0.03

580

Figure 1  
[Click here to download Figure: Figure 1.eps](#)

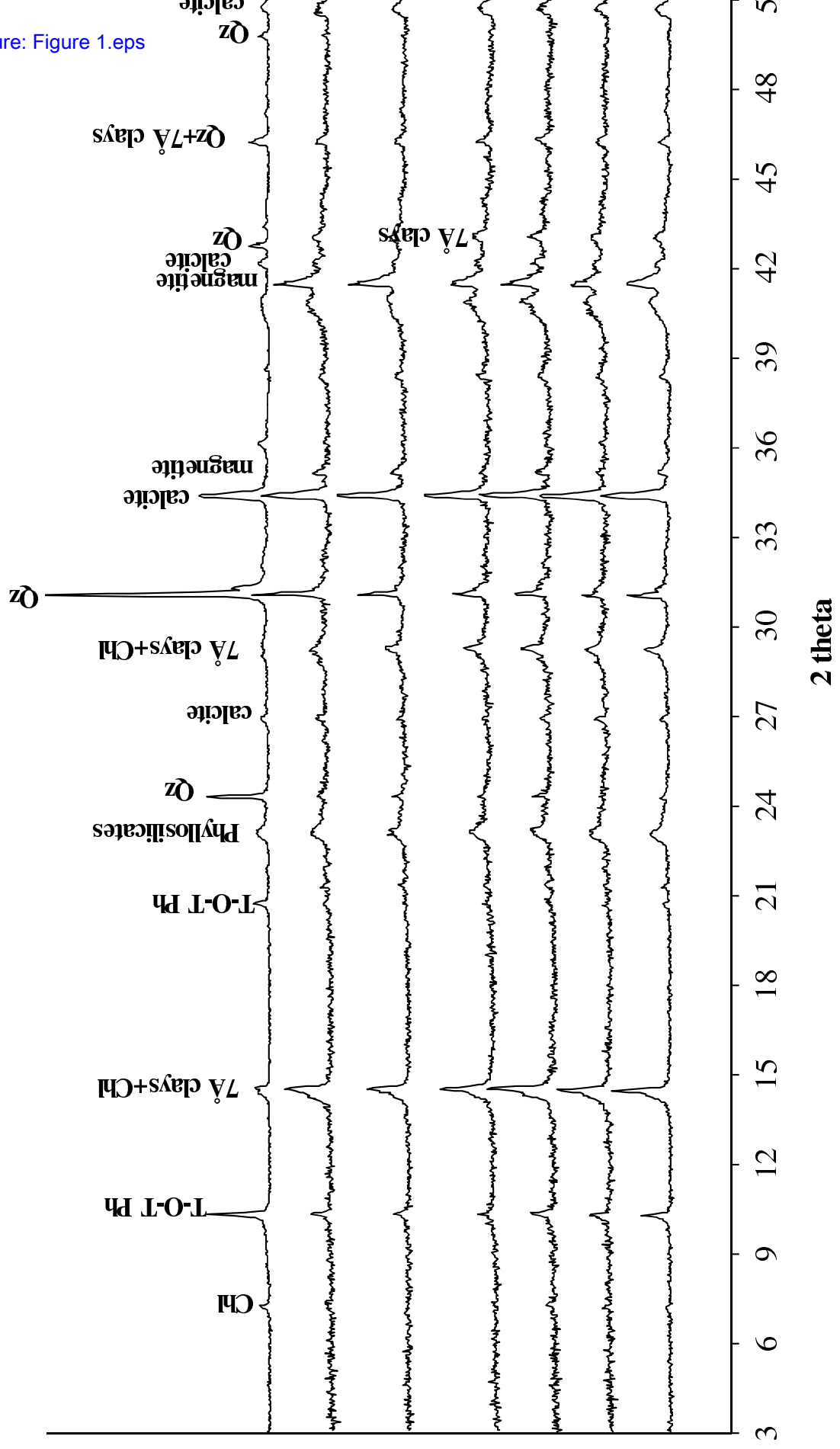


Figure 2  
[Click here to download Figure: Figure 2.eps](#)

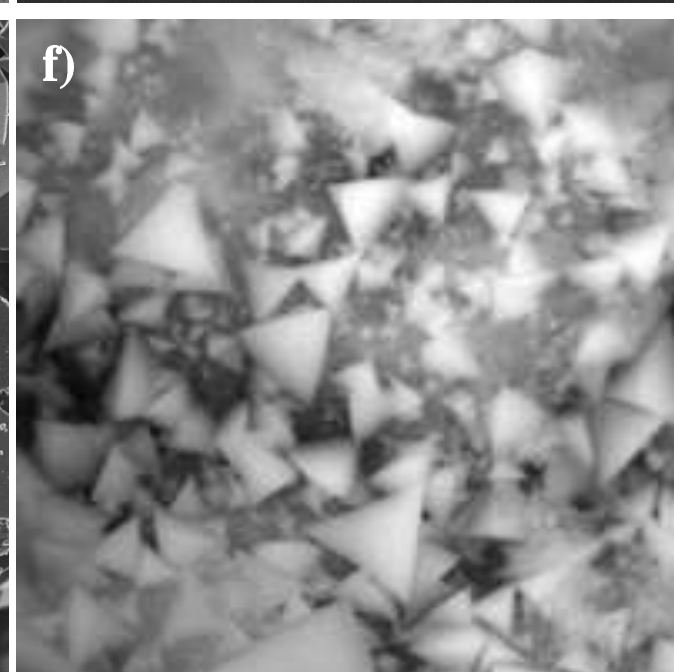
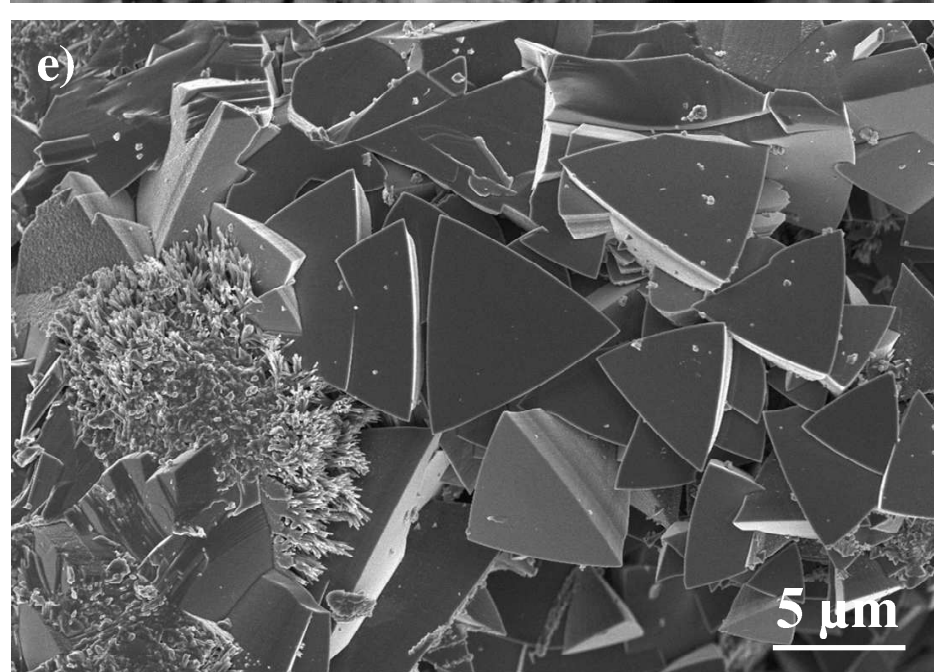
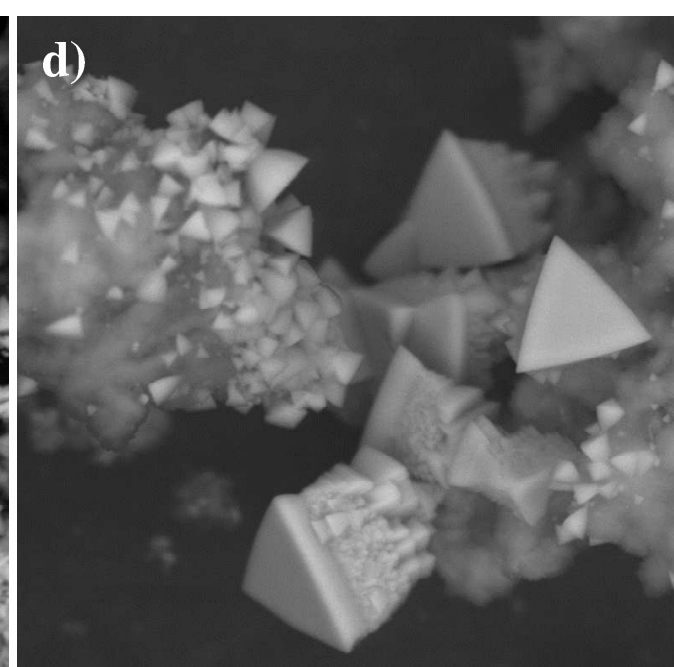
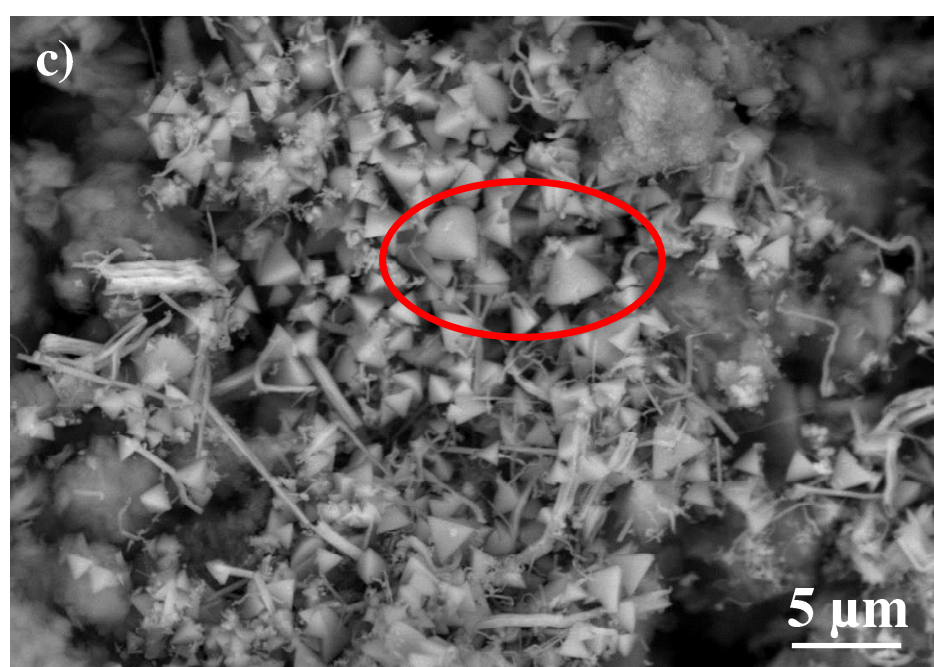
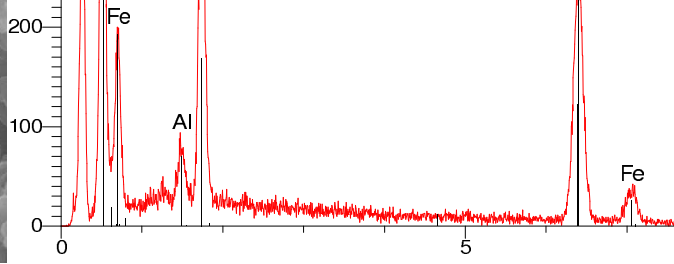
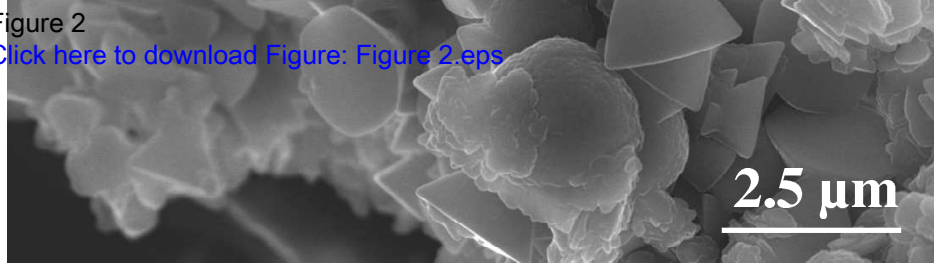


Figure 3

[Click here to download Figure: Figure 3 eps](#)

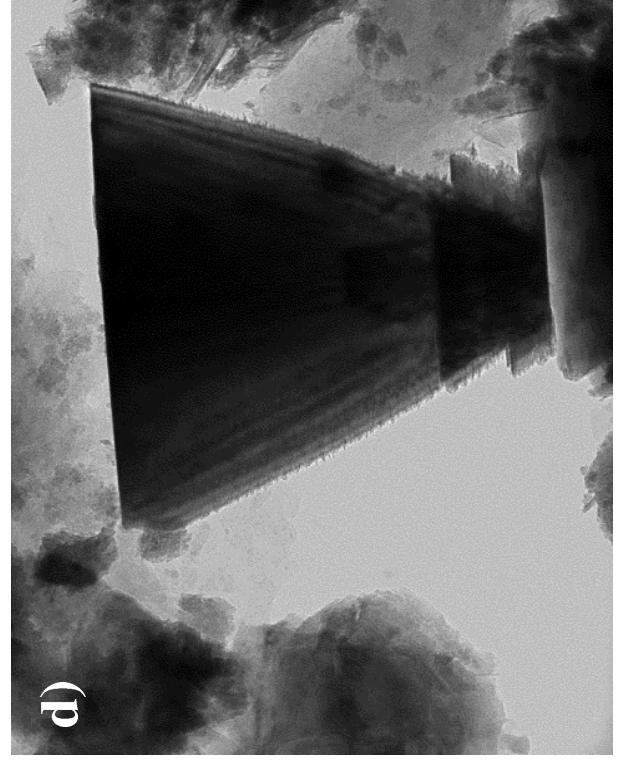
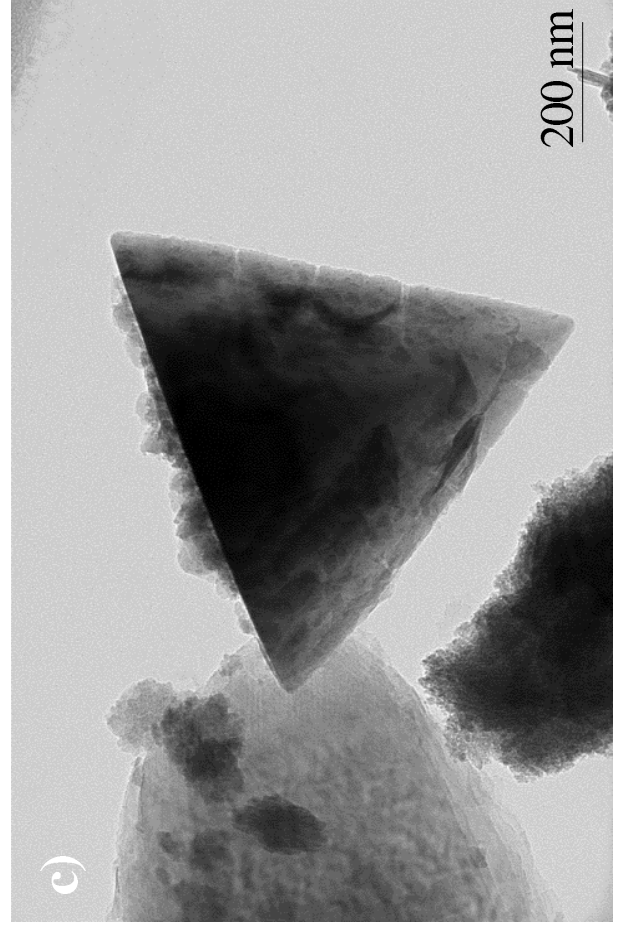
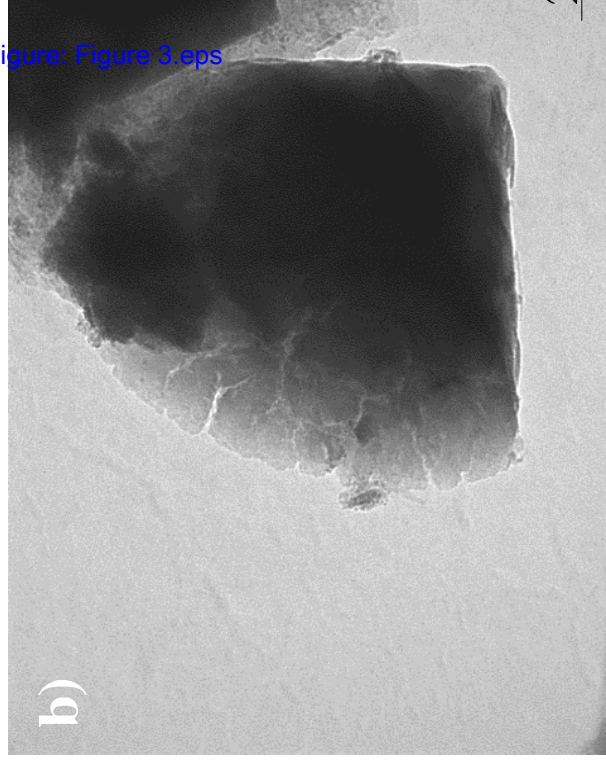
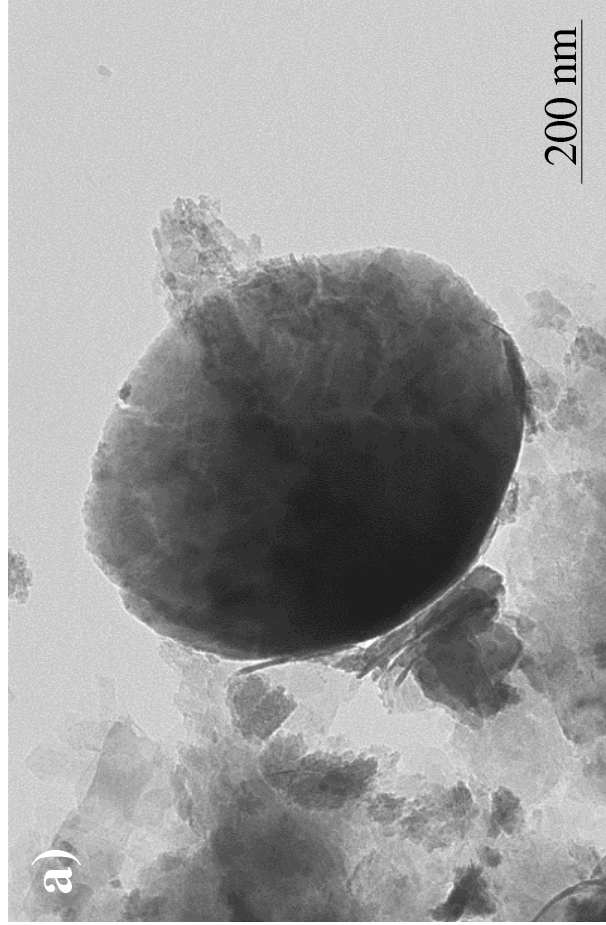


Figure 4

[Click here to download Figure: Figure 4.eps](#)

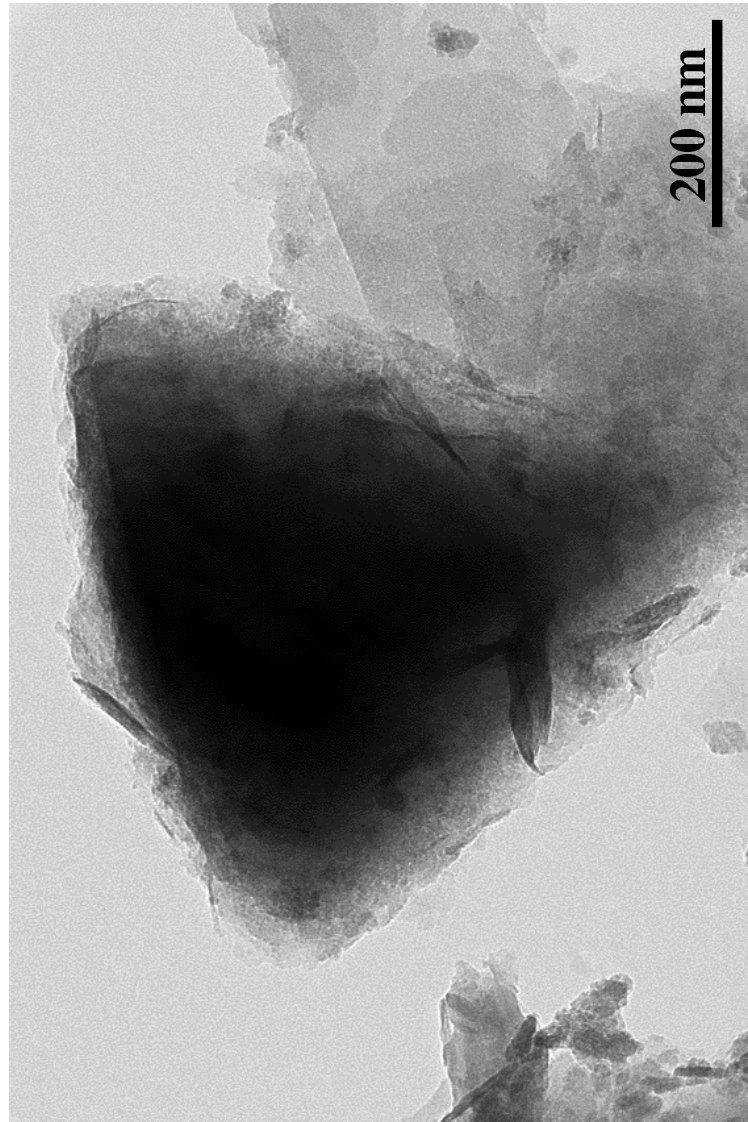


Figure 5

[Click here to download Figure: Figure 5.eps](#)

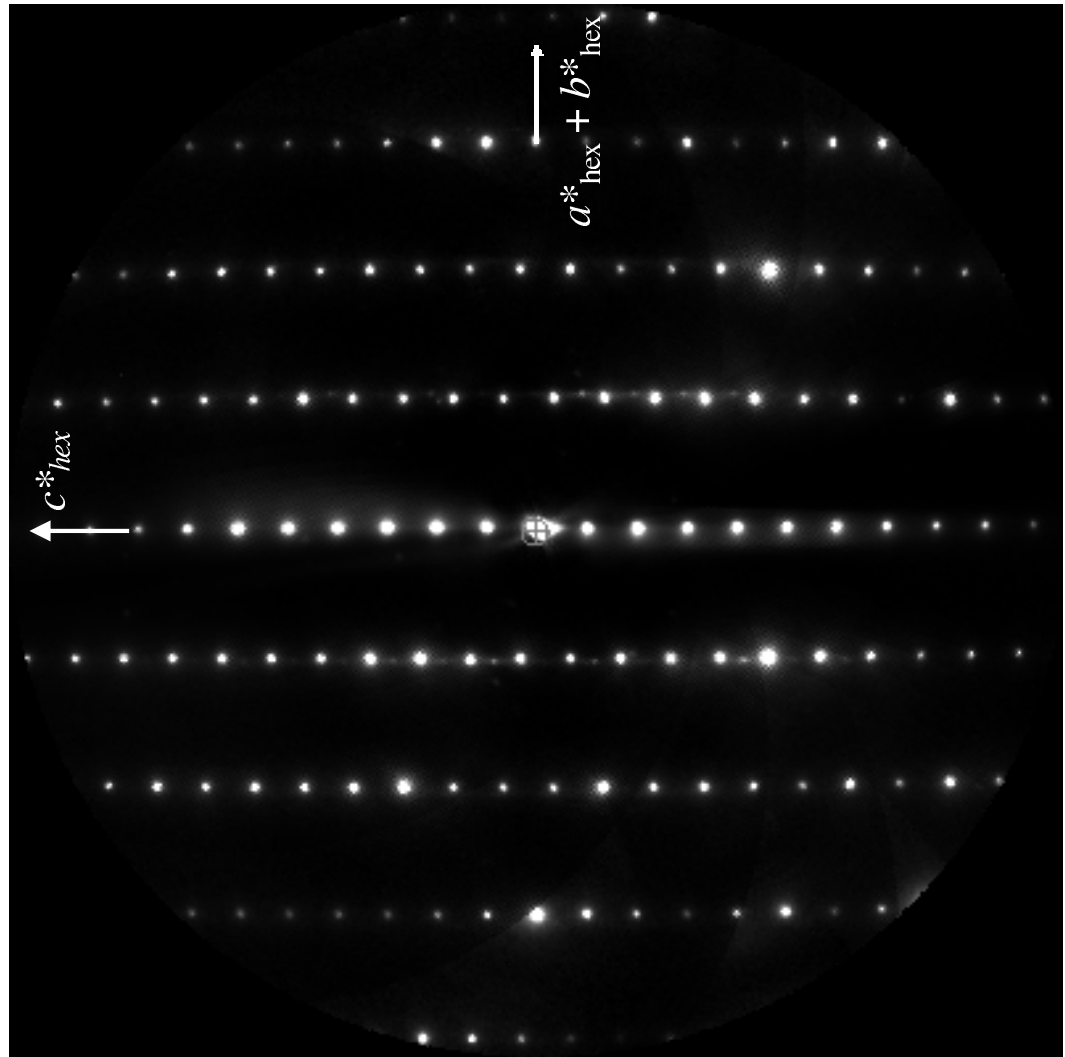


Figure 6

[Click here to download Figure: Figure 6.eps](#)

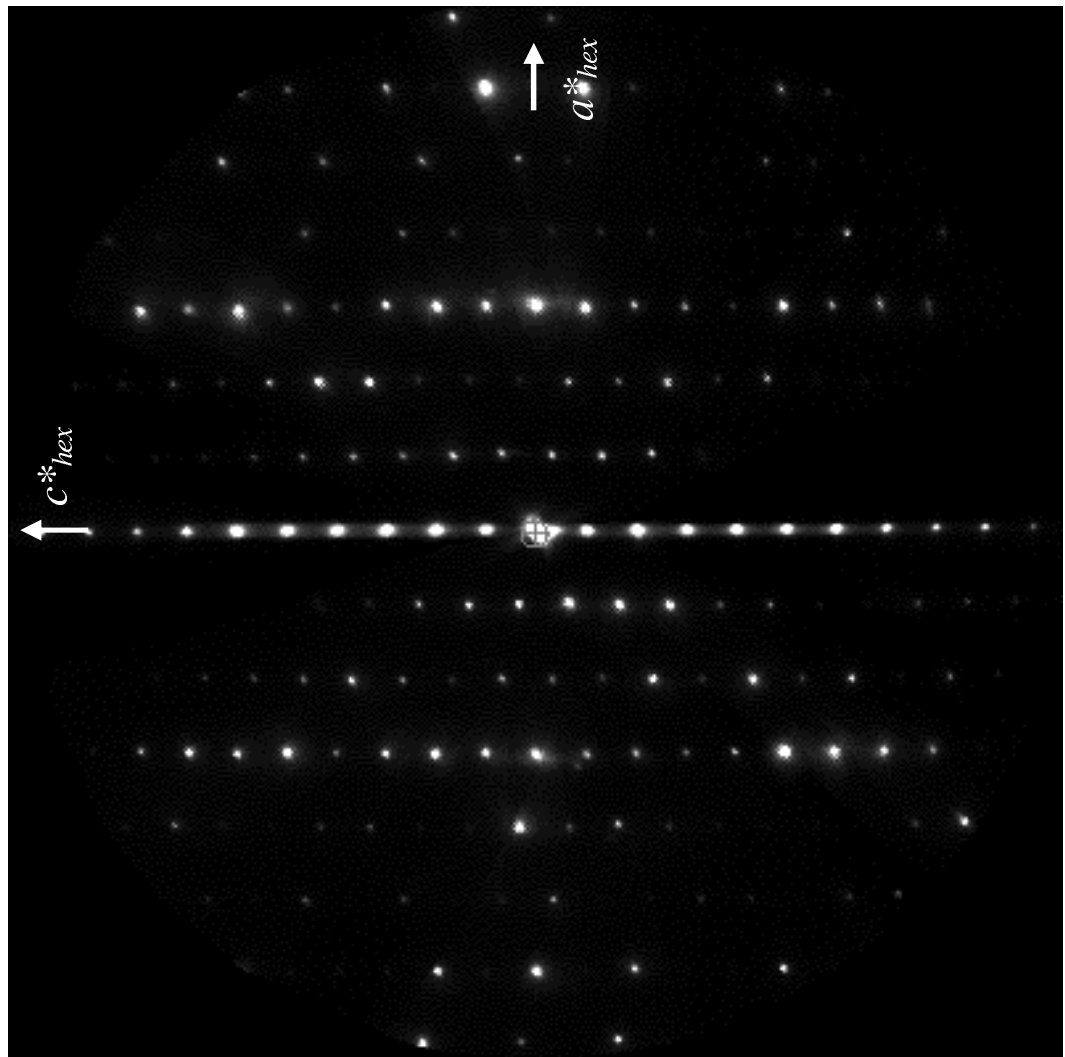
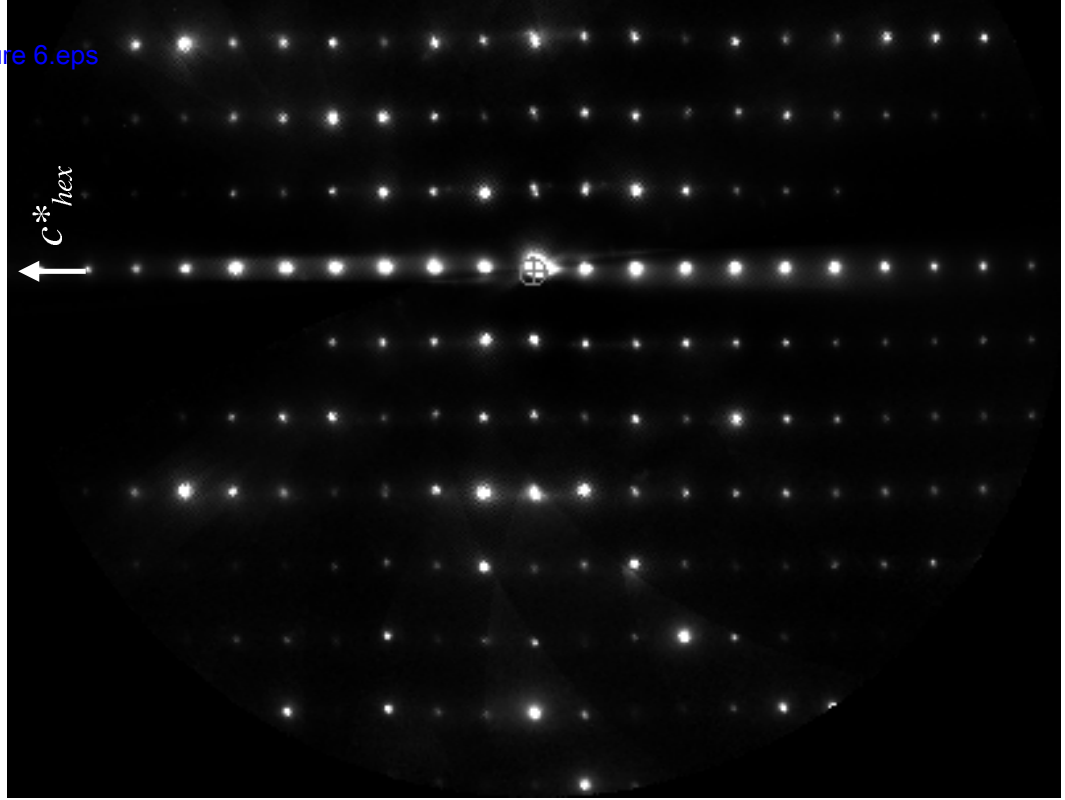


Figure 7  
[Click here to download Figure: Figure 7.eps](#)

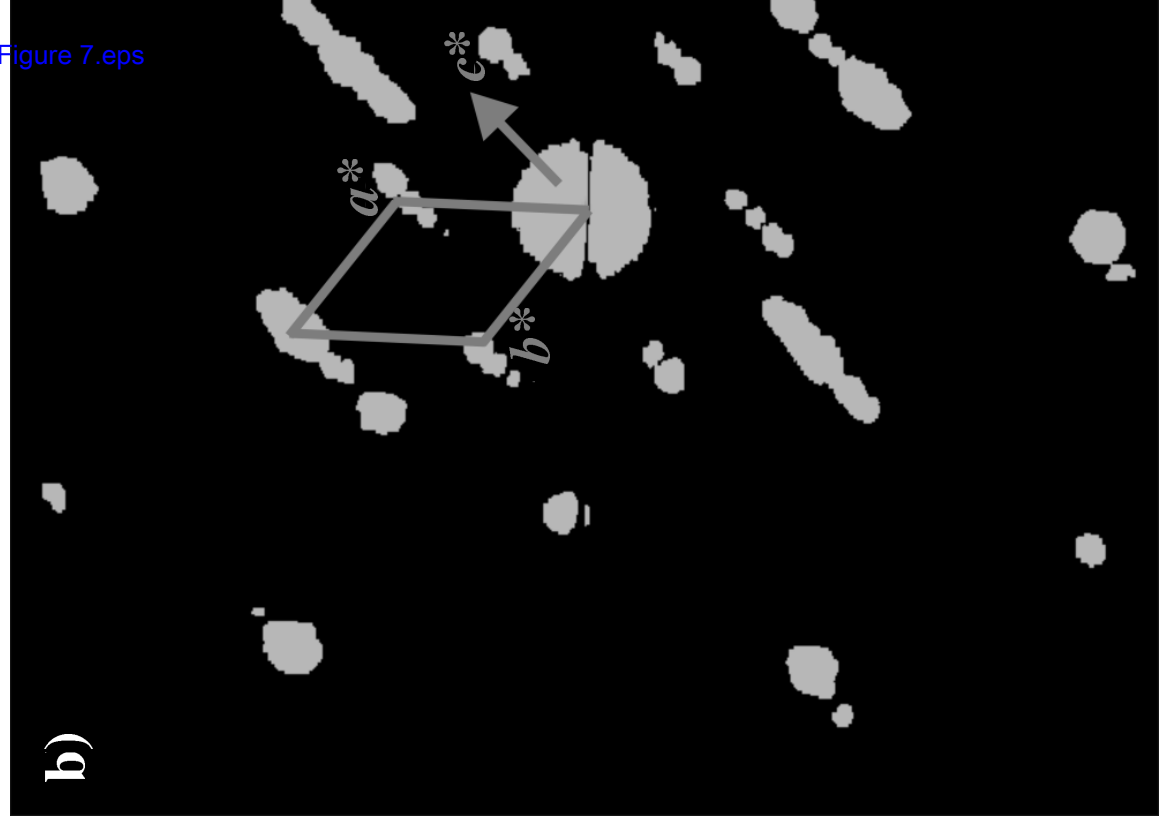
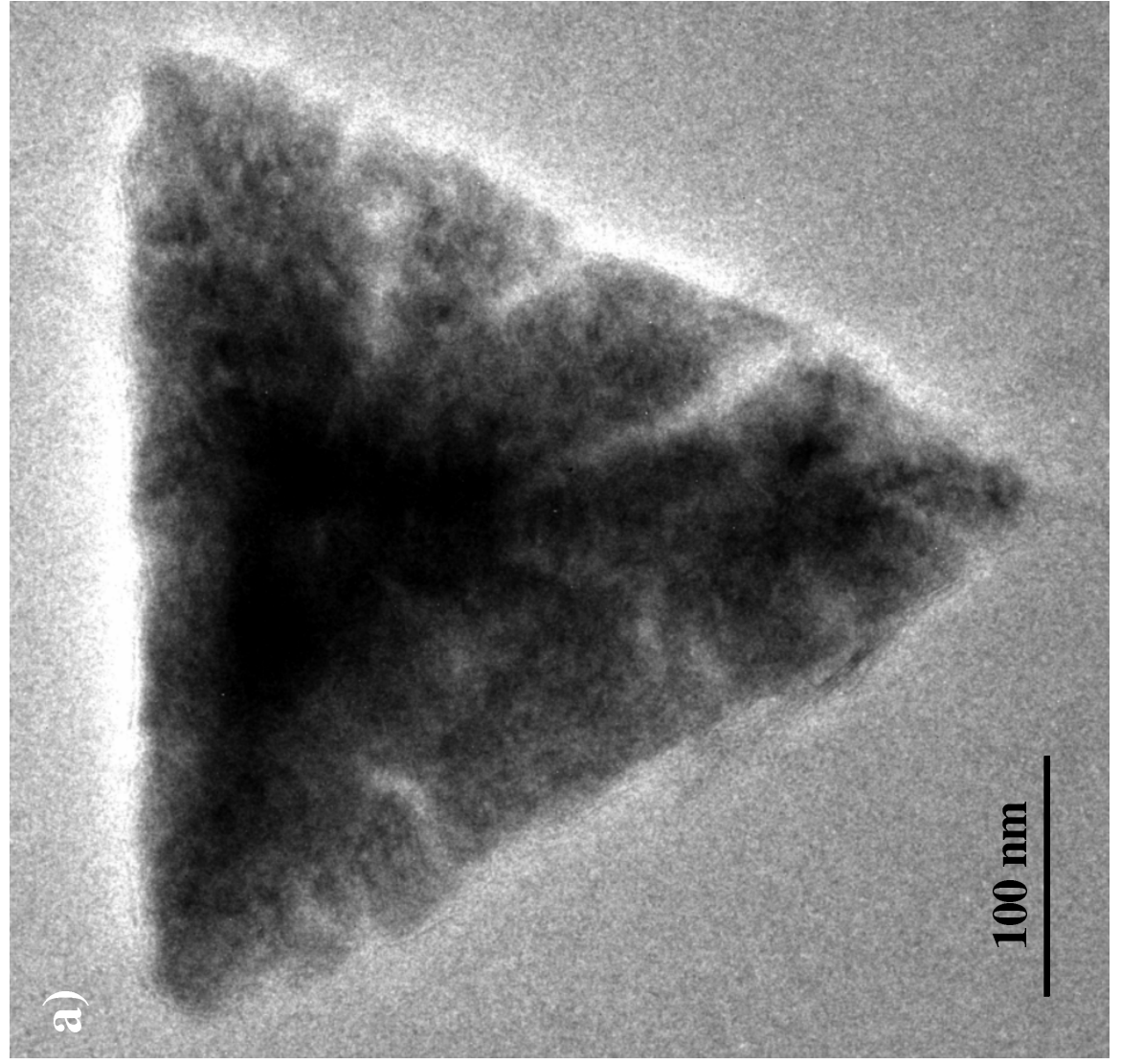


Figure 8  
[Click here to download Figure: Figure 8.eps](#)

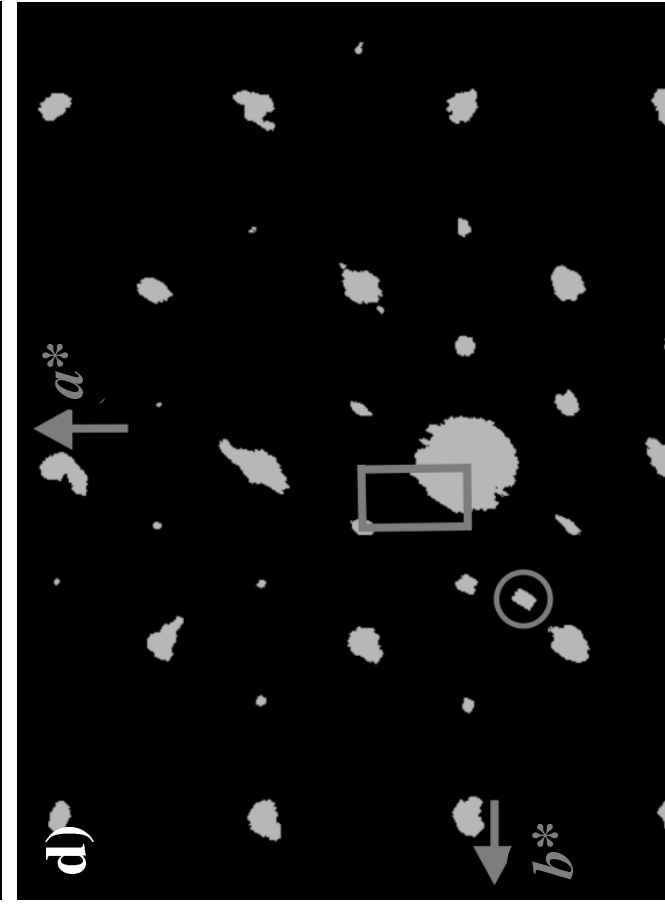
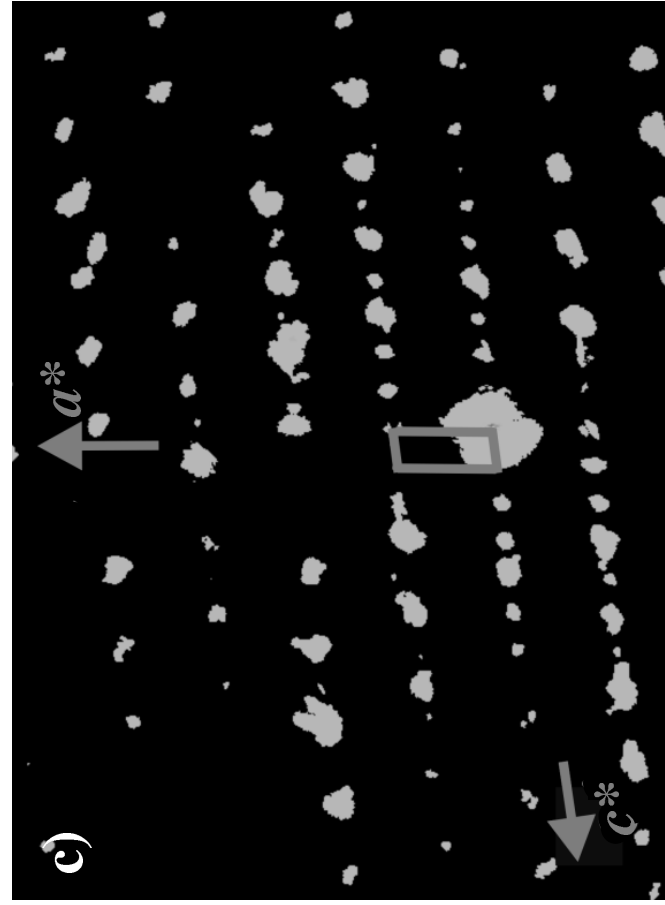
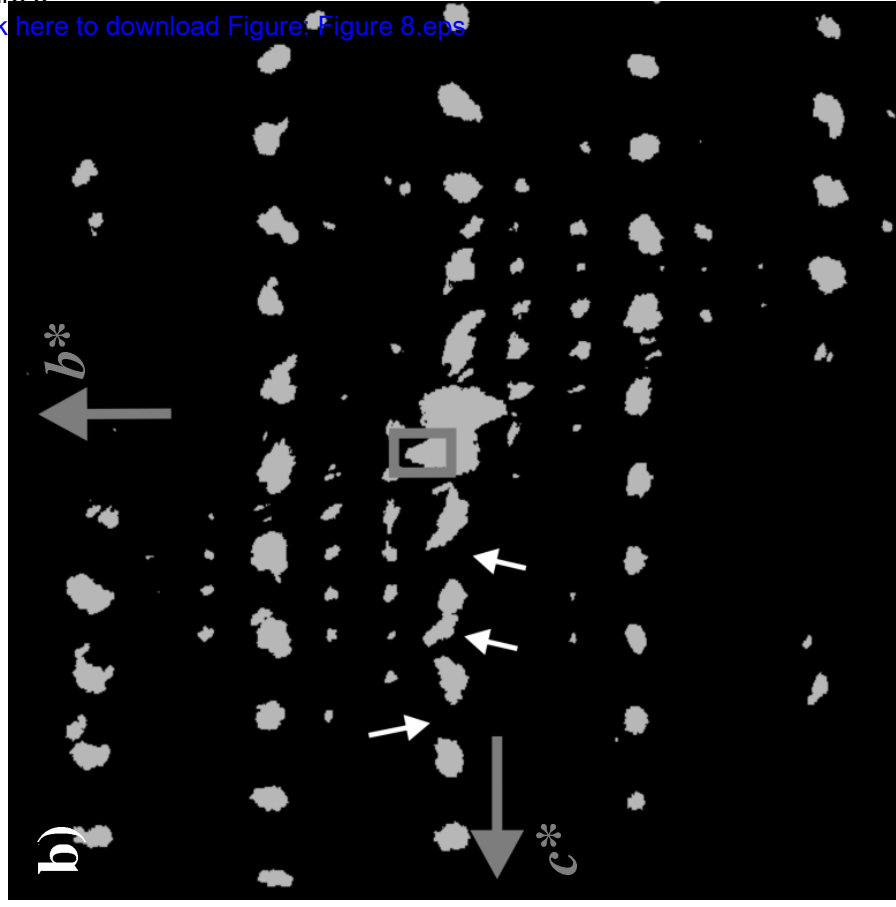
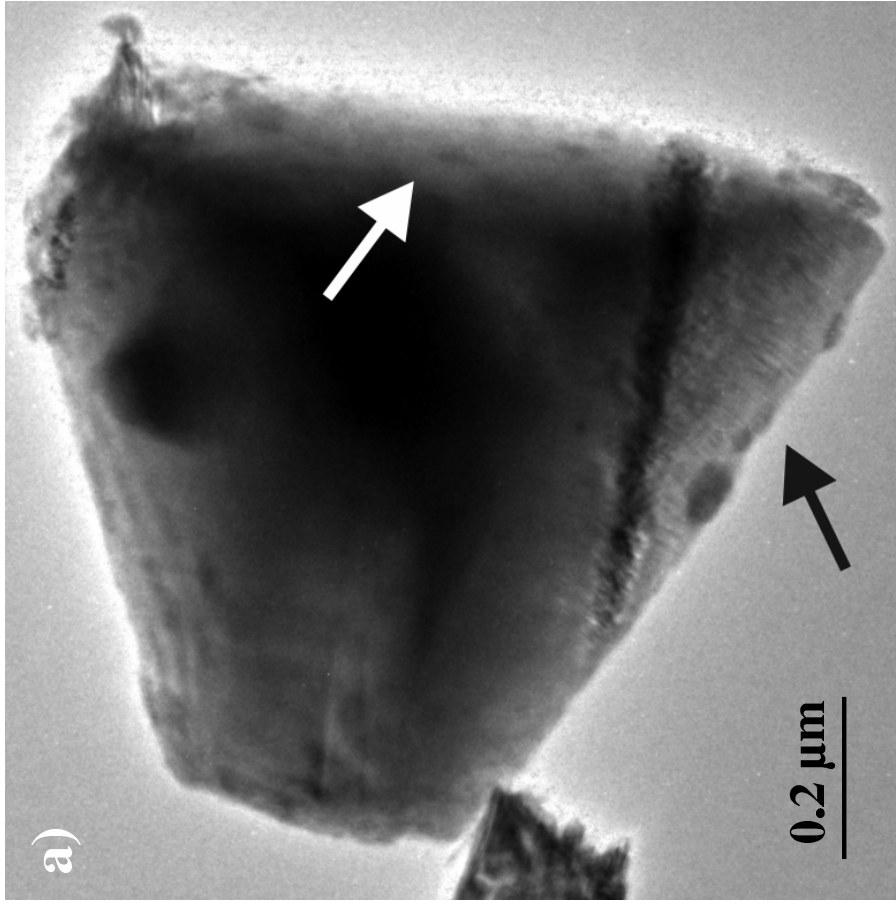


Figure 9  
[Click here to download Figure: Figure\\_9.eps](#)

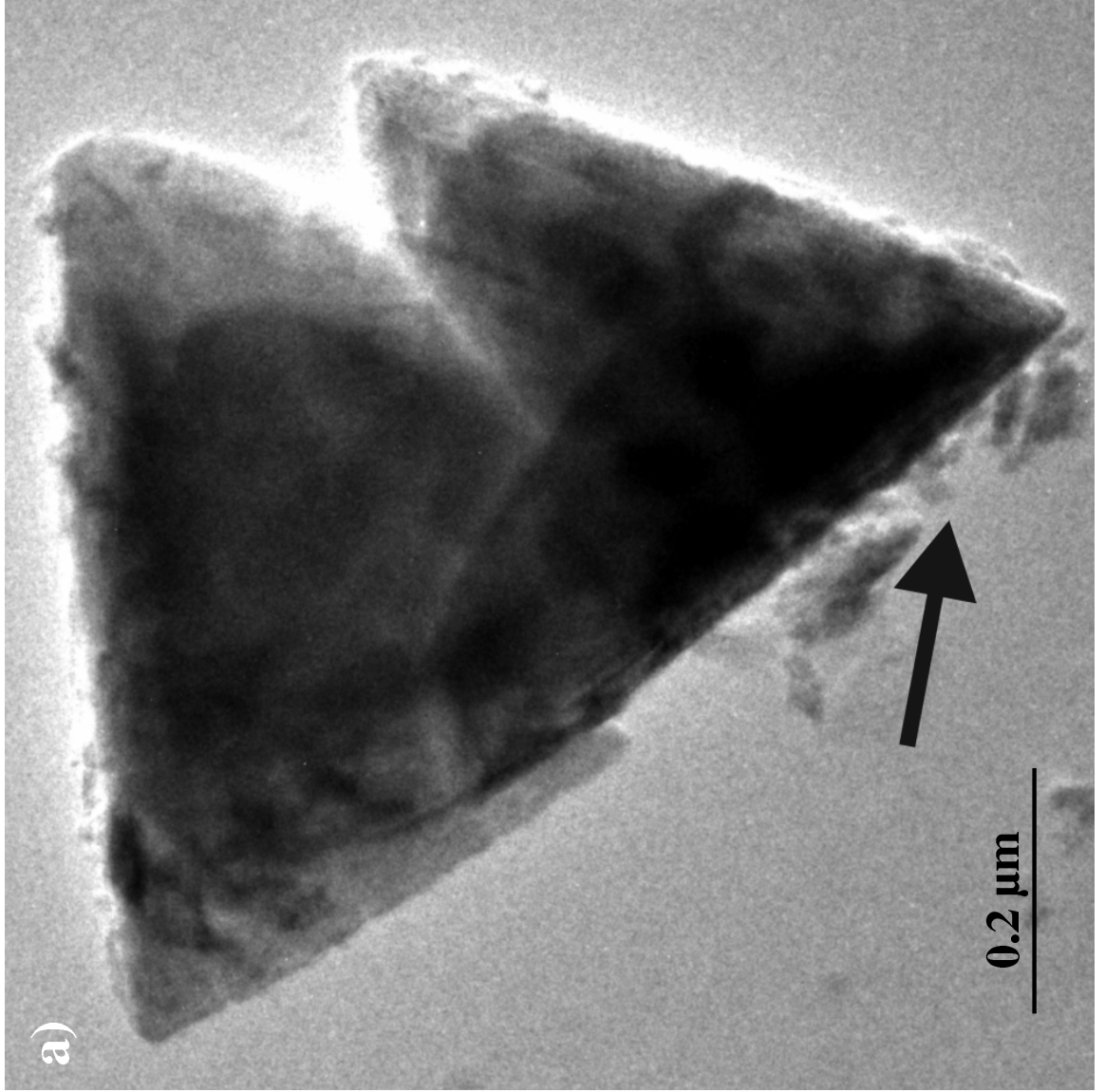


Figure 10

[Click here to download Figure: Figure 10.eps](#)

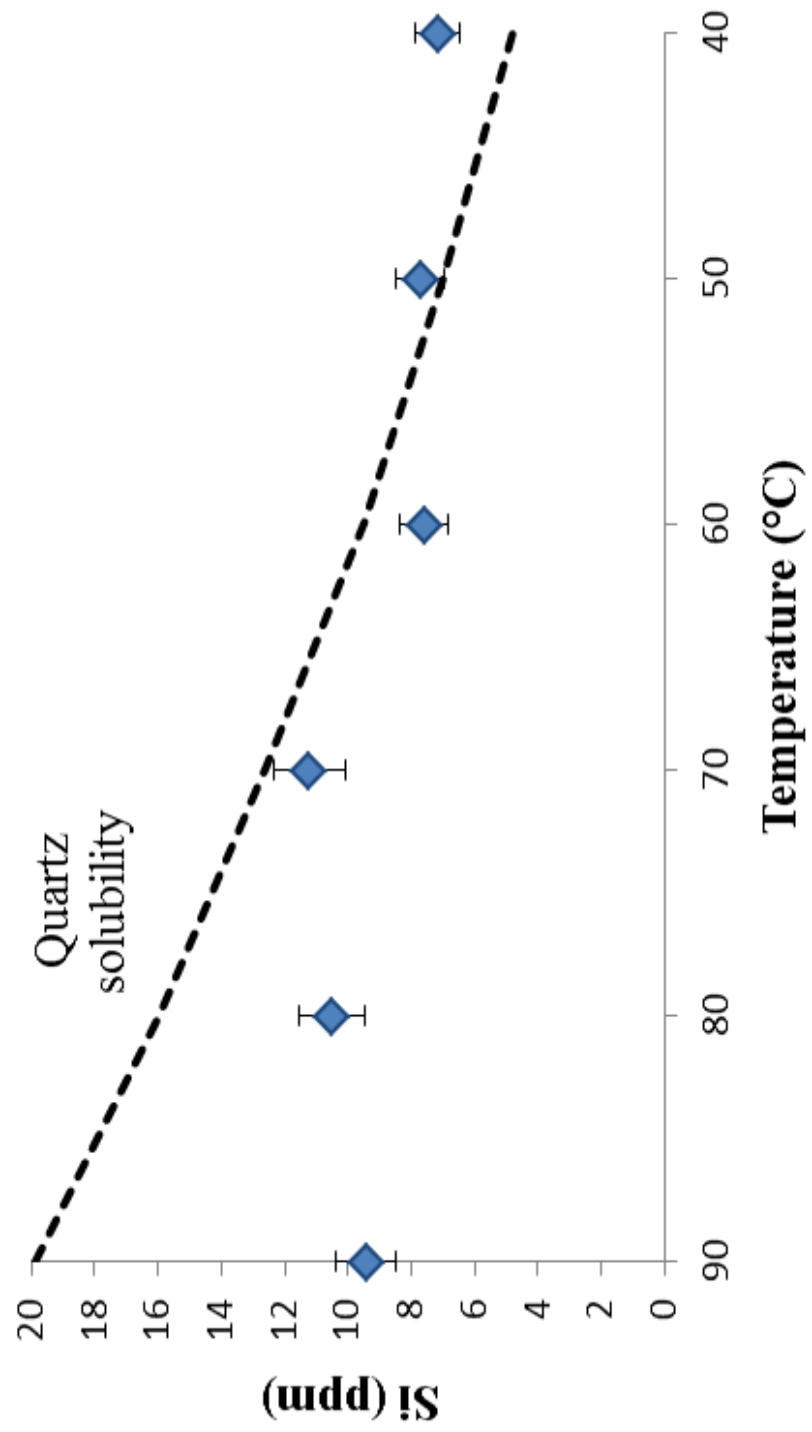


Figure 11  
[Click here to download Figure: Figure 11.eps](#)

